Rock Mechanics Bulletin 5 (2026) 100236

Contents lists available at ScienceDirect

Rock Mechanics Bulletin

journal homepage: www.keaipublishing.com/en/journals/rock-mechanics-bulletin

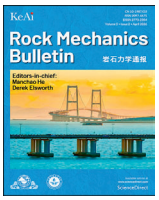

Full Length Article

Integrative solution of stress evolution in overburden roof strata during the coal seam mining by application of complex variable functions methodology

Yinkai Li[a], Hongwei Wang[a,c,*], Zhanbin Zhu[b], Daixin Deng[a,d], Naisheng Jiang[e]

[a] School of Mechanics and Civil Engineering, China University of Mining and Technology, Beijing, 100083, China
[b] Mataihao Coal Mine, Inner Mongolia Ordos Yongmei Mining Industry Co., Ltd., Ordos, 017212, China
[c] Joint National-Local Engineering Research Centre for Safe and Precise Coal Mining (Anhui University of Science and Technology), Huainan, 232001, China
[d] School of Mechanical Engineering, Sichuan University of Science and Engineering, Zigong, 643000, China
[e] School of Materials Science and Engineering, University of Science and Technology Beijing, Beijing, 100083, China

ARTICLE INFO

Keywords:
Overburden roof caving
Complex variable functions
Mechanical model
Stress evolution
Numerical simulation

ABSTRACT

Large-scale roof collapse is a major dynamic hazard threatening the safe coal mine operations. Understanding the deformation and failure characteristics of overburden rock strata, as well as deciphering the stress evolution mechanism of overburden rock structure in mining stopes, is of great theoretical advancement and engineering applications in roof disasters prevention. This study employs a theoretical derivation to systematically analyze the characteristics of overburden roof deformation and caving behavior during the coal seam mining. By modeling the trapezoidal caving zone in the overburden roof strata as a complex functional system, the stress distribution within the caving zone and adjacent intact strata was mathematically characterized. Stress evolution patterns of overburden strata at different caving stages were derived under both elastic and elastoplastic deformation conditions, accompanied by the demarcation of elastic-plastic zones. In addition, the critical length for the first caving and periodic caving of overburden are theoretically determined. To validate the proposed analytical framework, comprehensive numerical simulation and physical model tests are conducted to investigate the overburden roof caving characteristics during coal seam mining. Quantitative comparisons between experimental, numerical results and theoretical analyses were performed in terms of the caving range of roof strata, the critical length for the roof strata caving and stress distribution. The consistencies among different approaches confirms the reliability of the theoretical model, providing a robust foundation for optimizing mining designs and implementing effective roof control strategies.

1. Introduction

Coal seam mining is an essential industry that plays a crucial role in global energy production. However, the inherent risks associated with roof instability during the coal seam mining process can lead to sudden and catastrophic collapses of overburden roof. These accidents pose a significant threat to the safety of underground coal mines, often resulting in a large number of casualties and substantial property losses. Therefore, addressing roof instability has become a paramount concern in ensuring the safety and productivity of coal mine operations (Alejano et al., 2008; Alehossein and Poulsen, 2010; Deng, 2023; Jiang et al., 2014; Jiang and Zhao, 2015, 2017; Yuan et al., 2018; Wang et al., 2016, 2022). To mitigate these risks, it is crucial to develop an accurate mechanical model that can predict and understand the behavior of overburden roof caving. This research aims to present such a mechanical model.

Considerable efforts have been dedicated to extensive research on the mechanical mechanism of overburden rock movement, leading to a wealth of valuable research findings. In the current research results, beam and plate models are mainly used to analyze the stresses the stress of overburden rocks, for example, Qian et al. (1981, 1994) established a "voussoir beam" theory of overburden rock structure in fractured zone to achieve the quantitative description of the overburden roof movement. Based on this theory, the "key stratum" theory about rock

* Corresponding author.
E-mail address: whw@cumtb.edu.cn (H. Wang).
Peer review under the responsibility of Chinese Society for Rock Mechanics & Engineering.

https://doi.org/10.1016/j.rockmb.2025.100236
Received 11 April 2025; Received in revised form 7 June 2025; Accepted 9 August 2025
Available online 22 August 2025

movement was further proposed by Qian et al. (1996) to reveal the fracture mechanism of thick and hard overburden roof. Song (1994) proposed "transfer rock beam" theory through theoretical analysis based on a large number of coal mines on-site information, established the mechanical model of roof in stope with and without internal stress zone, and pointed that each rock block was hinged together through the contact point and played the role of force transfer after rock fracture. Huang (2002) established the short voussoir beam and step beam structural models in terms of the main roof periodic weighting, which provided a theoretical basis for the roof control in shallow buried coal seam. Xu et al. (2005) established the specific steps and methods for the identification of "key stratum" and analyzed the influence factors of the breaking sequence of two adjacent hard rock layers basing on the "key stratum" theory. Miao et al. (2021) pointed out the first fracture form of overburden rock with thick key stratum is arch, and the periodic fracture form is short block with unequal length. Kumar et al. (2015) pointed that the scale of overburden collapse area and the magnitude of ground subsidence were directly proportional to the mining height and both increased with the increase of mining height, which would greatly affect the behavior of goaf. Wen et al. (2011) proposed a stope spatial structure model based on the "transfer rock beam" theory and discussed the mechanical characteristics of the stress and structure part of the roof spatial structure. Deng (2023) constructed the mechanical models of different caving stages of overburden rock in stope, and obtained the solutions of the stress field evolution function solutions of overburden rock under elastic deformation and elastoplastic deformation. However, such models are limited to solving the stress within the deformation zone and are insufficient in characterizing the stress distribution of the intact rock layers outside.

The establishment of the roof model is actually aimed at accurately calculating the stress distribution within the roof. and analysing the stress distribution characteristics of the overburden roof during the coal seam mining is the key to achieve the prevention and control of roof accidents. In addition to the above theoretical analysis methods, numerical simulation and experimental methods are also applied. Le et al. (2018) presented a discontinuum modeling approach to investigate overburden roof caving behavior by analyzing the stress distribution in roof. Shen et al. (2020) conducted a three-dimensional numerical modeling to investigate the stress distribution during the coal seam mining and pointed out that the stress state near major geological structures is the key factor to induce the coal bursts in underground coal mine. Shabanimashcool and Li (2015) validated the bilinear truss model using UDEC, revealing that Young's modulus enhances buckling resistance but increases crushing failure risk, while horizontal in-situ stress regulates failure modes, providing a framework for stratified roof analysis. Huang (2007) conducted physical simulations using solid and solid-liquid medium models to investigate overburden movement and clay aquiclude stability in shallow coal mining, determining material properties through stress-strain and hydrophilic tests. Lou et al. (2021) investigated the progressive evolution of mining-induced stress by means of a large-scale physical modeling experiment and verified that the trajectories of principal stress are arch-shaped or inversely-arched, referred to as "principal stress arch". Therefore, the distribution characteristics of the stress field in the overburden roof can reflect a lot of information about the internal conditions of the roof during the coal seam mining. By analyzing the stress distribution in roof, it becomes possible to determine whether the roof is intact, whether cracks have developed, and whether the roof is prone to collapse.

Based on a lot of experimental findings and the field measurement, it has been observed that the overburden roof will form a trapezoidal zone when it deforms and collapses (Deng et al., 2023; Liu et al., 2018, 2021; Wang et al., 2023), as shown in Fig. 1. However, the existing theoretical analysis of the stress distribution of overburden roof deformation primarily relies on two types of mechanical models: the plate model and the rock beam model, which mainly study the stress distribution inside the range of deformation and collapse risk of the overburden roof. Therefore, in this paper, the complex functions model of overburden roof deformation in the trapezoidal zone is established. The establishment of the complex functions model not only solves the problem of stress evolution in the overburden caving area, but also obtains the stress distribution of the rock strata outside the overburden roof deformation and collapse area. At the same time, this paper establishes different

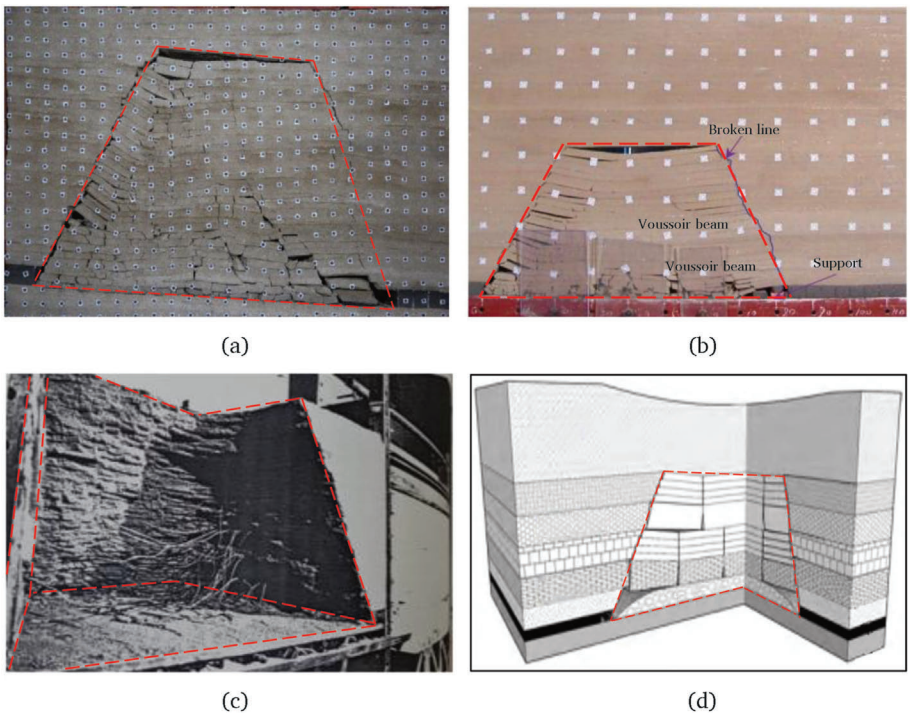

Fig. 1. The trapezoidal fracture zone of overburden roof. (a) The trapezoidal fracture zone from Deng et al. (2023); (b) The trapezoidal fracture zone from Liu et al. (2021); (c) The trapezoidal platform fracture zone from Liu et al. (2018); (d) The trapezoidal platform fracture zone from Wang et al. (2023).

superstatic beam mechanics models on the basis of the complex functions model, which are suitable for analyzing the first and periodic caving of overburden roof under the influence of mining, and the stress distribution in elastic deformation stage and plastic deformation stage of overburden roof are deduced. Moreover, the elastic-plastic boundary line and the distribution range of elastic zone and plastic zones in the overburden roof are determined as well. The critical length for the first caving and periodic caving of overburden are theoretically determined. It is beneficial to the safety management of mine roof and has great scientific significance for the early warning and prevention of roof dynamic disasters.

2. Complex functions model for deformation and caving of overburden roof strata

The overburden roof is generally composed of multiple discontinuous and natural geological layers with the characteristic of anisotropy and heterogeneity. However, considering the continuous deformation characteristics of rock strata under deep high confining pressure, the overburden can still be considered as a homogeneous, isotropic and continuous medium.

Based on the field measurement and some experimental findings, it has been observed that the overburden roof including the overburden roof above the mining face will form a trapezoidal fracture space when it deforms and collapses (Yang et al., 2016; Li et al., 2017; Xia et al., 2017; Lv et al., 2021). As the mining face advances, this fracture space will dynamically develop upward to the ground surface, causing the inner boundary of the fracture space to also dynamic development, as depicted in Fig. 2. Therefore, according to the deformation characteristics of the overburden strata after the caving space formation and the deformation characteristics of the overburden roof in the first and periodic caving, the complex functions mechanical model for deformation and collapse of the overburden roof is established in this study.

In this mechanical model, a rectangle is taken as a group of rock strata including floor strata, coal seam, overburden roof in underground coal mining. In order to obtain the stress distribution in the mechanical model, reasonable boundary conditions should be set around the model. Since the rectangle represents a part of rock stratum, zero vertical displacement is set at the base of model. The constant pressure q_1 is the vertical loading of the model in the y direction. The additional stress k ($q_1 + \rho gy$) induced by rock gravity is applied on the two side of model. k is the lateral pressure coefficient; ρ is the density of rock strata; g is the gravitational acceleration; l is the total advancement distance of the mining face; y_d is the height of the caving space of overburden roof above coal seam.

Through the establishment of the complex functions model for the overburden roof, not only the stress evolution in the overburden caving area is solved, but also the stress distribution of the rock strata outside the caving area is obtained. The core steps of the complex variable functions theory are as follows:

According to the complex variable functions theory, the area outside trapezoidal fracture space in the z plane (xy plane) should be transferred into a unit circle in the ζ plane by conformal mapping method, as shown in Fig. 2. The area outside trapezoidal fracture space in the z plane corresponds to that enclosed by the unit circle in the ζ plane. The conformal mapping of trapezoidal opening can be approximated with the following terms:

$$z = \omega(\zeta) = R\left(\frac{1}{\zeta} + c_1\zeta + c_3\zeta^3\right) \tag{1}$$

where ζ is a point in the unit circle; $\omega(\zeta)$ is conformal mapping function; R, c_1, c_3 are all real numbers, $R > 0$, $|c_1 + c_3| \le 1$, $c_1 = \cos 2k_2\pi$, $c_3 = \frac{1}{6}\sin^2 2k_2\pi$, k_2 is a mathematical parameter related to the ratio of the length l, and the height y_d, calculated by $\frac{1+c_1+c_3}{1-c_1+c_3} = \frac{l}{y_d}$.

At the infinite distance of the surrounding rock in trapezoidal opening, it can be obtained from the boundary conditions:

$$\left.\begin{aligned} B_d &= \frac{1}{4}(\sigma_1 + \sigma_2) \\ B' + \mathrm{i}C' &= -\frac{1}{2}(\sigma_1 - \sigma_2)\mathrm{e}^{-2\mathrm{i}\beta} \end{aligned}\right\} \tag{2}$$

where β is an intersection angle between maximum principal stress σ_1 and x axis.

Complex functions $f_o(\sigma)$ of boundary conditions expression on unit circle is listed below:

$$\begin{aligned} f_o(\sigma) = \mathrm{i}\int(\overline{f_x} + \mathrm{i}\overline{f_y})\mathrm{d}s - \frac{\overline{F_x} + \mathrm{i}\overline{F_y}}{2\pi}\ln\sigma - \frac{1+\mu}{8\pi}\left(\overline{F_x} - \mathrm{i}\overline{F_y}\right)\frac{\omega(\sigma)}{\overline{\omega'(\sigma)}}\sigma \\ -2B_d\omega(\sigma) - (B' - \mathrm{i}C')\overline{\omega(\sigma)} \end{aligned} \tag{3}$$

where μ is Poisson's ratio, $\overline{f_x}$, $\overline{f_y}$ are the surface force component along the x direction, y direction on the boundary of the trapezoidal opening, $\overline{F_x}$, $\overline{F_y}$ are the sum of $\overline{f_x}$ and $\overline{f_y}$, respectively.

And with regard to the boundary condition of the unit circle, com-

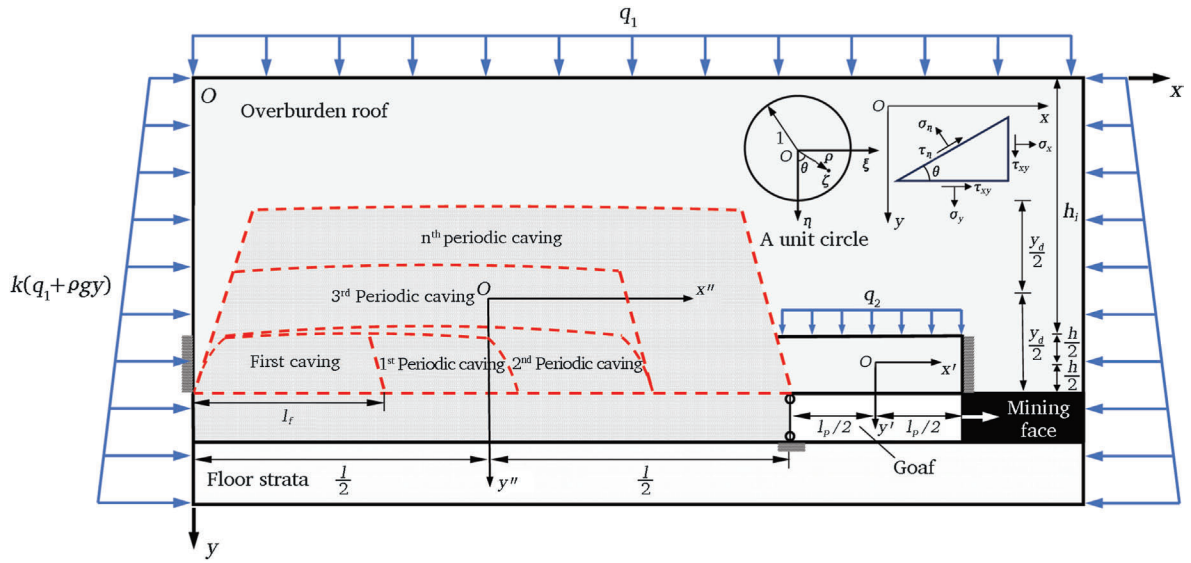

Fig. 2. Complex functions model for deformation and caving of overburden roof.

plex functions $\varphi_o(\zeta)$ and $\varphi_o(\zeta)$ can be expressed as follows:

$$\left.\begin{aligned}\varphi_o(\zeta)&=\frac{1}{2\pi i}\int_\sigma\frac{f_o(\sigma)}{\sigma-\zeta}d\sigma-\frac{1}{2\pi i}\int_\sigma\frac{\omega(\sigma)}{\overline{\omega'(\sigma)}}\frac{\overline{\varphi_o'(\sigma)}}{\sigma-\zeta}d\sigma\\ \psi_o(\zeta)&=\frac{1}{2\pi i}\int_\sigma\frac{\overline{f_o(\sigma)}}{\sigma-\zeta}d\sigma-\frac{1}{2\pi i}\int_\sigma\frac{\overline{\omega(\sigma)}}{\omega'(\sigma)}\frac{\varphi_o'(\sigma)}{\sigma-\zeta}d\sigma\end{aligned}\right\}\tag{4}$$

The two complex potential functions are listed below:

$$\left.\begin{aligned}\varphi(\zeta)&=\frac{1+\mu}{8\pi}\left(\overline{F_x}+i\overline{F_y}\right)\ln\zeta+B_d\omega(\zeta)+\varphi_o(\zeta)\\ \psi(\zeta)&=-\frac{3-\mu}{8\pi}\left(\overline{F_x}-i\overline{F_y}\right)\ln\zeta+(B'+iC')\omega(\zeta)+\psi_o(\zeta)\end{aligned}\right\}\tag{5}$$

where B_d, B', C' are constants, determined by the principal stress σ_1 and σ_2 in the infinite distance of the mechanical model.

The stress components of the area outside trapezoidal orifice in the plane problem can be determined by two analytic complex functions $\Phi(\zeta)$ and $\Psi(\zeta)$.

$$\left.\begin{aligned}(\sigma_x)_d+(\sigma_y)_d&=4\mathrm{Re}[\Phi(\zeta)]\\ (\sigma_y)_d-(\sigma_x)_d+2i(\tau_{xy})_d&=\frac{2}{\omega'(\zeta)}[\overline{\omega(\zeta)}\Phi'(\zeta)+\omega'(\zeta)\Psi(\zeta)]\end{aligned}\right\}\tag{6}$$

where Re is the real part of a complex function, the x direction normal stress, y direction normal stress and shear stress of rock strata outside trapezoidal orifice of overburden roof fracture zone are $(\sigma_x)_d$, $(\sigma_y)_d$, $(\tau_{xy})_d$.

It is evident that during the mining of coal seam, the overburden roof undergoes a progressive suspension, as the area of the overburden trapezoidal deformation and collapse risk zone steadily expands, the first caving of the overburden roof will occur. Prior to the occurrence of the first caving, the overburden roof can be considered as a statically indeterminate beam with two fixed boundaries according to the complex functions model. Following the first caving of the overburden roof, the area of the trapezoidal zone further increases during the mining of coal seam, the periodic caving of the overburden roof will occur, and the left side of the roof beam above the mining face is released. As the caved rock mass undergoes complete fragmentation and expansion, the broken rock masses offer vertical support to the overburden roof. As a result, the previously fixed boundary on the left side is transformed into a hinged support. Without considering the influence of hydraulic supports around the mining face, the model can be considered as containing one fixed boundary and one hinged boundary according to the complex functions model.

3. Stress distribution in overburden roof

3.1. Stress calculation in overburden roof by complex functions model

Based on the core steps of the complex variable functions theory, the stress distribution of the rock strata outside the trapezoidal fracture space can be obtained. Combine the boundary conditions of the mechanical model, constants B_d, B', C' are obtained by Eq. (2):

$$\left.\begin{aligned}B_d&=\frac{1}{4}(q_1+k(q_1+\rho gy))\\ B'&=\frac{1}{2}(k(q_1+\rho gy)-q_1)\\ C'&=0\end{aligned}\right\}\tag{7}$$

Since there is no force around the trapezoidal opening boundary, the surface force components are all zero, that is:

$$\overline{f_x}=\overline{f_y}=0,\overline{F_x}=\overline{F_y}=0\tag{8}$$

There is $\sigma=\zeta$ on the boundary of the unit circle, Eq. (9) can be transformed from Eq. (1):

$$\left.\begin{aligned}&\omega(\sigma)=R\left(\frac{1}{\sigma}+c_1\sigma+c_3\sigma^3\right),\omega'(\sigma)=R\left(-\frac{1}{\sigma^2}+c_1+3c_3\sigma^2\right)\\ &\overline{\omega(\sigma)}=R\left(\sigma+\frac{c_1}{\sigma}+3c_3\sigma^{-3}\right),\overline{\omega'(\sigma)}=R\left(-\sigma^2+c_1+3c_3\sigma^{-2}\right)\\ &\frac{\omega(\sigma)}{\overline{\omega'(\sigma)}}=-\sigma\frac{c_3\sigma^4+c_1\sigma^2+1}{\sigma^4-c_1\sigma^2-3c_3}=-c_3\sigma-\frac{(1+c_3)c_1\sigma^3+(1+3c_3{}^2)\sigma}{\sigma^4-c_1\sigma^2-3c_3}\\ &\frac{\overline{\omega(\sigma)}}{\omega'(\sigma)}=\frac{1}{\sigma}\frac{\sigma^4+c_1\sigma^2+c_3}{3c_3\sigma^4+c_1\sigma^2-1}=\frac{1}{3c_3\sigma}\left[1+\frac{(3c_3-1)c_1\sigma^2+(3c_3{}^2+1)}{3c_3\sigma^4+c_1\sigma^2-1}\right]\end{aligned}\right\}\tag{9}$$

where σ is the boundary value of the unit circle.

and then from Eqs. (3), (7)–(9), it can be obtained that:

$$f_o(\sigma)=-2B_d\omega(\sigma)-B'\overline{\omega(\sigma)}\tag{10}$$

Because $\varphi_o(\zeta)$ is an analytic function with single value in the unit circle, it can be assumed that: $\varphi_o(\zeta)=\alpha_1\zeta+\alpha_2\zeta^2+\alpha_3\zeta^3+\cdots+\alpha_n\zeta^n=\sum_{k=1}^{\infty}\alpha_k\zeta^k$, where α_1, α_2, α_3, etc. are complex constants, $\frac{1}{2\pi i}\int_\sigma\frac{\omega(\sigma)}{\overline{\omega'(\sigma)}}\frac{\overline{\varphi_o'(\zeta)}}{\sigma-\zeta}d\sigma=-c_3(\overline{\alpha_1}\zeta+2\overline{\alpha_2})$, $\frac{1}{2\pi i}\int_\sigma\frac{f_o(\sigma)}{\sigma-\zeta}d\sigma=-2B_dR(c_1\zeta+c_3\zeta^3)-B'R\zeta$, they are substituted into Eq. (4) and compared the coefficients of the same power terms of ζ on both sides of the equation, the specific form of $\varphi_o(\zeta)$ is as follows:

$$\varphi_o(\zeta)=\left(\frac{2B_dRc_1+B'R}{c_3-1}\right)\zeta-2B_dRc_3\zeta^3\tag{11}$$

further, $\frac{1}{2\pi i}\int_\sigma\frac{\overline{\omega(\sigma)}}{\omega(\sigma)}\frac{\varphi_o'(\sigma)}{\sigma-\zeta}d\sigma=\alpha_1c_4+3\alpha_3\left(\frac{\zeta^5+c_1\zeta^3+c_3\zeta}{3c_3\zeta^4+c_1\zeta^2-1}\right)$, $c_4=-\frac{(3c_3{}^2-1)\zeta^3+(c_3-1)c_1\zeta-2c_3\frac{1}{\zeta}}{3c_3\zeta^4+c_1\zeta^2-1}$, $\frac{1}{2\pi i}\int_\sigma\frac{\overline{f_o(\sigma)}}{\sigma-\zeta}d\sigma=-2B_dR\zeta-B'R(c_1\zeta+c_3\zeta^3)$, they are substituted into Eq. (10), the specific form of $\psi_o(\zeta)$ is as follows:

$$\psi_o(\zeta)=-2B_dR\zeta-B'R\left(c_1\zeta+c_3\zeta^3\right)+\alpha_1c_4-3\alpha_3\left(\frac{\zeta^5+c_1\zeta^3+c_3\zeta}{3c_3\zeta^4+c_1\zeta^2-1}\right)\tag{12}$$

According to Eqs. (5), (11) and (12), the specific form of $\Phi(\zeta)$, $\Psi(\zeta)$ are as follows:

$$\left.\begin{aligned}\varphi(\zeta)&=B_dR\left(\frac{1}{\zeta}+c_1\zeta+c_3\zeta^3\right)+\left(\frac{2B_dRc_1+B'R}{c_3-1}\right)\zeta-2B_dRc_3\zeta^3\\ \psi(\zeta)&=B'R\left(\frac{1}{\zeta}+c_1\zeta+c_3\zeta^3\right)+\psi_o(\zeta)\end{aligned}\right\}\tag{13}$$

then it can be obtained that:

$$\left.\begin{aligned}\varphi'(\zeta)&=B_dR\left(-\frac{1}{\zeta^2}+c_1+3c_3\zeta^2\right)+\frac{2B_dRc_1+B'R}{c_3-1}-6B_dRc_3\zeta^2\\ \psi'(\zeta)&=B'R\left(-\frac{1}{\zeta^2}+c_1+3c_3\zeta^2\right)+\psi_o'(\zeta)\end{aligned}\right\}\tag{14}$$

and from Eq. (5), some formulas can be transformed:

$$\left.\begin{aligned}\omega'(\zeta)&=R\left(-\frac{1}{\zeta^2}+c_1+3c_3\zeta^2\right)\\ \overline{\omega(\zeta)}&=R\left(\frac{1}{\rho^2}\zeta+\frac{c_1\rho^2}{\zeta}+c_3\rho^6\zeta^{-3}\right)\end{aligned}\right\}\tag{15}$$

the two analytic complex functions are list:

$$\left.\begin{aligned}\Phi(\zeta)&=\varphi'(\zeta)/\omega'(\zeta)\\ \Psi(\zeta)&=\psi'(\zeta)/\omega'(\zeta)\end{aligned}\right\}\tag{16}$$

according to Eqs. (5), (14)–(16), the two complex potential functions $\Phi(\zeta)$, $\Psi(\zeta)$ are as follows:

$$\left.\begin{aligned}\Phi(\zeta) &= B_d + \left(\frac{2B_dRc_1 + B'R}{c_3 - 1} - 6B_dRc_3\zeta^2\right) \Big/ \left(-\frac{1}{\zeta^2} + c_1 + 3c_3\zeta^2\right) \\ \Psi(\zeta) &= \psi'(\zeta) \Big/ \omega'(\zeta) = B' + \psi'_o(\zeta) \Big/ R\left(-\frac{1}{\zeta^2} + c_1 + 3c_3\zeta^2\right)\end{aligned}\right\} \tag{17}$$

further, it can be obtained that:

$$\Phi'(\zeta) = \left[-12B_dc_3\zeta\left(-\frac{1}{\zeta^2} + c_1 + 3c_3\zeta^2\right) - \left(\frac{2B_dRc_1 + B'}{c_3 - 1} - 6B_dc_3\zeta^2\right)\left(\frac{2}{\zeta^3} + 6c_3\zeta\right)\right] \Big/ \left(-\frac{1}{\zeta^2} + c_1 + 3c_3\zeta^2\right)^2 \tag{18}$$

Finally, Eqs. (15), (17) and (18) are substituted into Eq. (6), the stress components of the area outside trapezoidal orifice can be obtained.

In order to analyze the stress distribution characteristics of the rock strata outside the trapezoidal fracture space, the geological conditions of 21221 mining face of Qianqiu coal mine in Henan province, China is taken as the engineering. The density ρ of the mudstone is set as 2500 kg/m^3, and the gravitational acceleration g is set as 9.8 m/s^2. The parameters φ and c are set as 30°, 2 MPa that represent internal friction angle and cohesion of rock stratum respectively.

According to the derivation process of stress distribution of complex functions model, the length and width of the caving region and the external boundary loading conditions need to be determined for stress analysis. Due to the uncertainty range of overburden fracture areas, the different ratios $w = l/y_d$ of model length to height of overburden fracture areas is selected to analyze the stress distribution characteristics.

Fig. 3 shows the stress components distribution of the overburden along the horizontal direction when the vertical height of the overburden is aligned with the location of the center of the fracture zone (specific cross section $y = y_d/2$) under different ratios of model length to height in the complex functions model of overburden roof deformation. With the increase of the horizontal distance from the boundary of fracture zone, the stress components σ_x, σ_y, τ_{xy}, σ_θ distribution of overburden roof all firstly increase and then gradually decrease, and finally stay stable and almost unchanged. The peak of stress components σ_x, σ_y, τ_{xy}, σ_θ all present obviously increase with the increase of ratios of model length to height.

With the decrease of the horizontal distance from the boundary of fracture zone, overburden roof initially forms a yield point. The location of this yield point can be determined by the yield criterion. Specifically, the Mohr-Coulomb yield criterion is adopted as the yield criterion of rock strata:

$$\sigma_1 = \frac{1 + \sin\varphi}{1 - \sin\varphi}\sigma_3 + \frac{2c\cos\varphi}{1 - \sin\varphi} \tag{19}$$

where σ_1, σ_3 are the maximum principal stress and minimum principal stress, respectively, which can be calculated by the stress components. And the Mohr stress circle can be plotted with σ_1, σ_3.

Express the Mohr-Coulomb yield criterion in terms of general stress components:

$$k_2(\sigma_x + \sigma_y)^2 - k_3(\sigma_x + \sigma_y) + m^2 - k_4\left[(\sigma_x - \sigma_y)^2 + 4(\tau_{xy})^2\right] = 0 \tag{20}$$

where $k_1 = \frac{1+\sin\varphi}{1-\sin\varphi}$, $m_1 = \frac{2c\cos\varphi}{1-\sin\varphi}$, $k_2 = (1 - k_1)^2$, $k_3 = 4m_1(1 - k_1)$, $k_4 = (1 + k_1)^2$.

The variation of τ_0 with σ_0 at the initial yield point can be calculated by Eq. (21).

$$\left.\begin{aligned}\sigma_0 &= \frac{1}{2}(\sigma_x + \sigma_y) - \sqrt{(\sigma_x - \sigma_y)^2 + 4(\tau_{xy})^2}\sin\varphi_0 \\ \tau_0 &= \sqrt{(\sigma_x - \sigma_y)^2 + 4(\tau_{xy})^2}\cos\varphi_0\end{aligned}\right\} \tag{21}$$

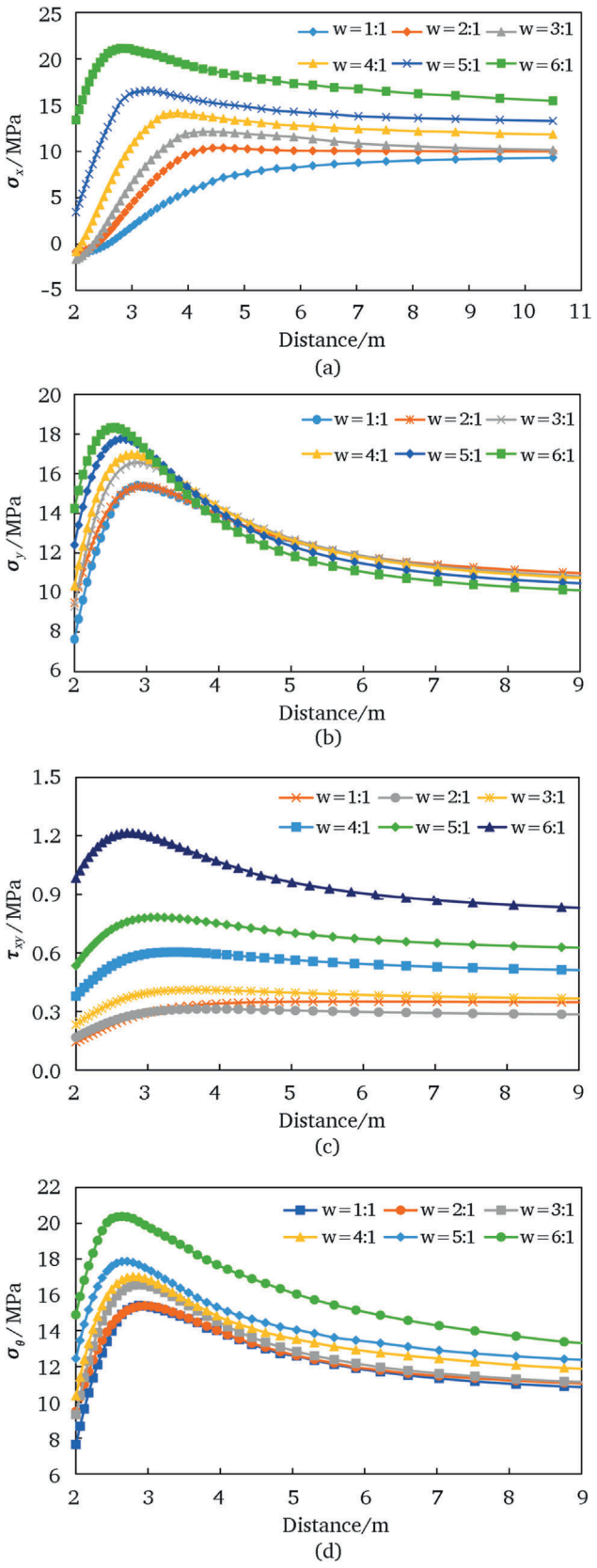

Fig. 3. The distribution of stress components in the overburden roof under different ratios of model length to height. (a) The σ_x distribution along horizontal direction; (b) The σ_y distribution along horizontal direction; (c) The τ_{xy} distribution along horizontal direction; (d) The σ_θ distribution along horizontal direction.

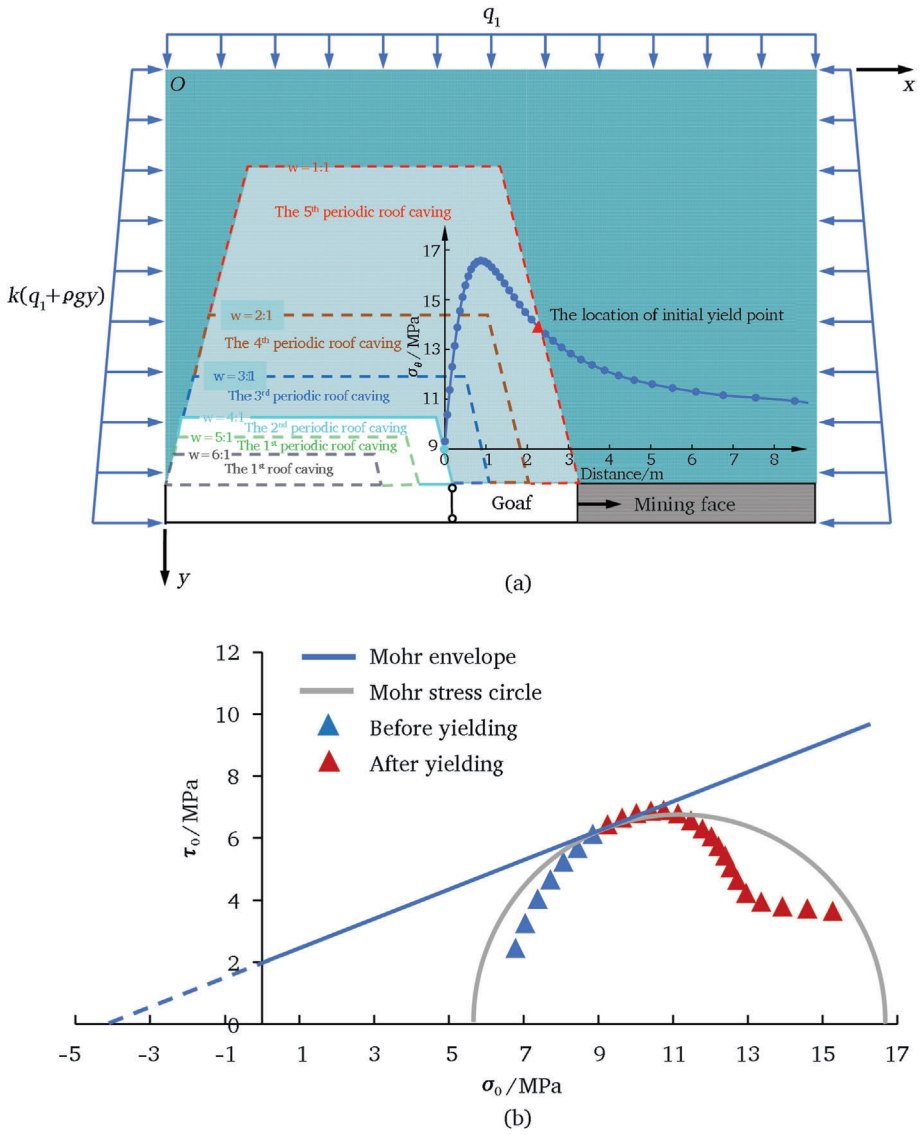

Fig. 4. The variation of τ_0 with σ_0 at the initial yield point in the complex functions model of the overburden roof when $w = 4{:}1$. (a) The location of initial yield point of overburden roof when $w = 4{:}1$; (b) The variation of τ_0 with σ_0 at the initial yield point.

where σ_0 is the normal stress, τ_0 is the shear stress, φ_0 is the orientation of the shear plane.

When the lateral pressure coefficient $k = 1.2$, Fig. 4 demonstrates the location of initial yield point and the variation of τ_0 with σ_0 at the initial yield point in the complex functions model of the overburden roof when $w = 4{:}1$. As shown in Fig. 4, the Mohr stress circle is tangent to the Mohr envelope at this point, indicating that the point is in a plastic equilibrium state and has begun to fail. With the increase of the normal stress σ_0, the shear stress τ_0 firstly increases, then decreases, and finally stabilizes with minimal variation. The trend of the stress distribution at the initial yield point remains essentially the same as the trajectory of the Mohr stress circle until it reaches yield and τ_0 begins to decrease.

As shown in Fig. 5, when the vertical height of the overburden is aligned with the location of the center of the fracture zone (specific cross section $y = y_d/2$), with the increase of the horizontal distance from the center of the fracture zone, σ_x and τ_{xy} firstly increase slowly and then become stable, σ_y and σ_θ increase rapidly to the peak value and then decrease slowly to stable state. As the increase of lateral pressure coefficient, the peak of stress component σ_x presents obviously increase, σ_y, τ_{xy} and σ_θ both present obviously decrease.

While the ratio of model length to height $w = 3{:}1$, Fig. 6 presents the location of initial yield point and the variation of τ_0 with σ_0 at the initial yield point in the complex functions model of the overburden roof when $k = 1.5$. As shown in Fig. 6, the Mohr stress circle cuts through the Mohr envelope at this point, indicating that the point has undergone failure. With the increase of the normal stress σ_0, the shear stress τ_0 also firstly increases, then decreases, and finally stays stable and almost unchanged. The trend of the stress distribution at the initial yield point remains essentially the same as the trajectory of the Mohr stress circle until it reaches yield and τ_0 starts to decline.

3.2. Stress calculation in overburden roof during the first caving

As previously discussed, according to the complex functions model, the mechanical model of the overburden roof during the first caving can be treated as a statically indeterminate beam with two fixed boundaries. At both ends of this beam structure, vertical reaction forces and bending moments exist simultaneously. Therefore, the principle of superposition is employed to decompose the statically indeterminate system into the combination of two statically determinate structures, as illustrated in

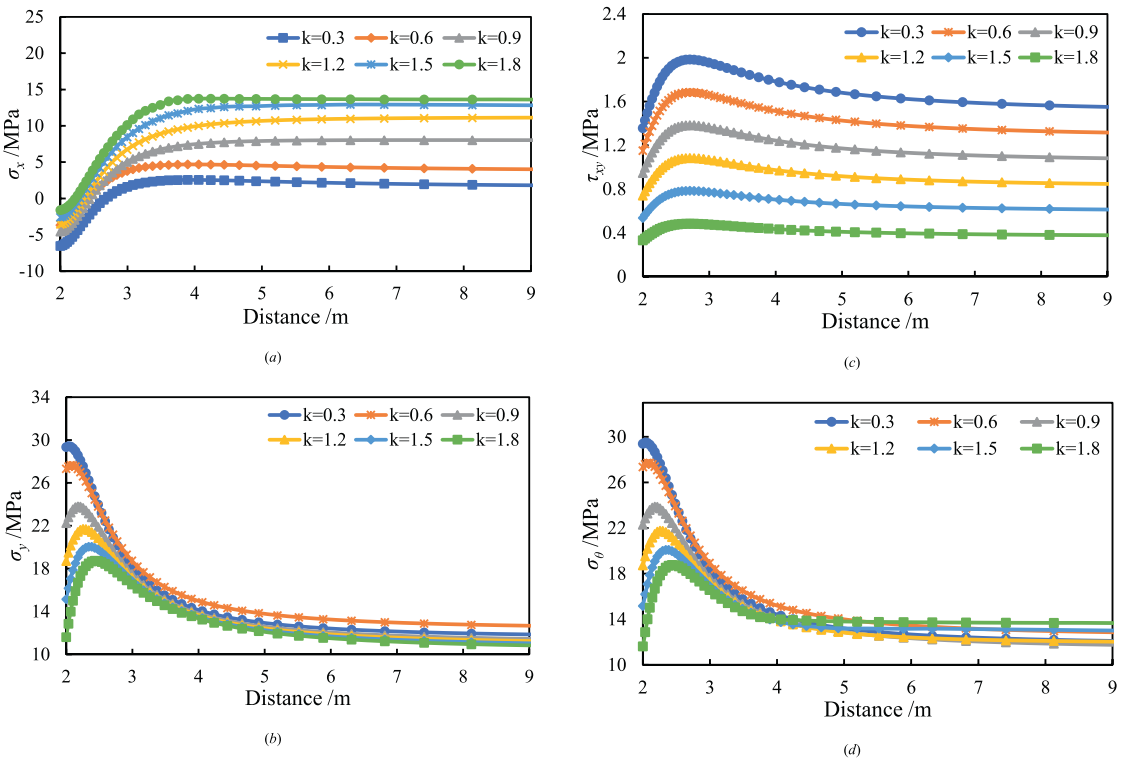

Fig. 5. Influence of shear stress τ_{xy} in overburden roof under different lateral pressure coefficients. (a) The σ_x distribution along horizontal direction; (b) The σ_y distribution along horizontal direction; (c) The τ_{xy} distribution along horizontal direction; (d) The σ_θ distribution along horizontal direction.

Fig. 7. In this model, the roof gravity is considered into surface force by equivalent substitution. The parameter q_2 is the gravity of rock strata above the roof; h is the thickness of immediate roof above the coal seam; h_i is the thickness of overburden roof above the immediate roof; l_f is the advancement distance of the mining face when the first caving of immediate roof occurs.

The stress components in the elastic stage of overburden roof can be obtained by elastic mechanics theory (Xu, 2016):

$$\left.\begin{aligned}\left(\sigma_x^e\right)_f &= \frac{(2q_2+\gamma h)}{h^3}\left[\left(\frac{{l_f}^2}{4}-3x^2-\frac{3h^2}{10}\right)y+2y^3\right]\\ \left(\sigma_y^e\right)_f &= -\frac{(2q_2+\gamma h)}{4h^3}\left(h^3-3h^2y+4y^3\right)-\gamma y\\ \left(\tau_{xy}^e\right)_f &= -\frac{(6q_2+3\gamma h)}{h^3}x\left(\frac{h^2}{4}-y^2\right)\end{aligned}\right\} \tag{22}$$

where γ represents the unit weight of gravity for the roof, in the elastic stage the x direction normal stress, y direction normal stress and shear stress of statically indeterminate beam of the overburden roof during the first caving are $(\sigma_x^e)_f$, $(\sigma_y^e)_f$, $(\tau_{xy}^e)_f$.

With the progressive increase of mining face advancement length, the roof overhang length l_f also increases, the roof gradually enters the elastoplastic deformation state from the elastic deformation state. There is a critical length for the overhanging length of the roof, and the stress components of the roof must meet Mohr-Coulomb yield criterion are shown in Eq. (20).

In addition, according to the deformation characteristics of statically indeterminate beam, the boundary point ($x = 0$; $y = 0.5h$) in statically indeterminate beam first enters the plastic state. By substituting the stress obtained from Eq. (21) at the boundary point ($x = 0$; $y = 0.5h$) into Eq. (22), the critical length l_f of the roof can be listed as follows:

$$l_f = \sqrt{\frac{8\mathrm{m}_1 h^2}{2q_2+pgh}-0.8h^2} \tag{23}$$

where m_1 is a constant, $m_1 = \frac{2c\cos\varphi}{1-\sin\varphi}$.

The stress will be redistributed after some areas of rock strata enter the plastic deformation state, and the plastic stress components need to satisfy the equilibrium differential equation:

$$\left.\begin{aligned}\frac{\partial\left(\sigma_x^p\right)_f}{\partial x}+\frac{\partial\left(\tau_{xy}^p\right)_f}{\partial y}&=0\\ \frac{\partial\left(\sigma_y^p\right)_f}{\partial y}+\frac{\partial\left(\tau_{xy}^p\right)_f}{\partial x}+\gamma&=0\end{aligned}\right\} \tag{24}$$

where the x direction normal stress, y direction normal stress and shear stress of statically indeterminate beam of the overburden roof during the first caving in the plastic stage are $(\sigma_x^p)_f$, $(\sigma_y^p)_f$, $(\tau_{xy}^p)_f$, respectively.

There must be a function $\Phi(x,y)$ where $(\sigma_x^p)_f = \frac{\partial^2\Phi}{\partial y^2}$, $(\sigma_y^p)_f = \frac{\partial^2\Phi}{\partial x^2}-\gamma y$, $(\tau_{xy}^p)_f = -\frac{\partial^2\Phi}{\partial x\partial y}$ are presented. It can be assumed that the function $\Phi(x,y)$ is:

$$\Phi(x,y) = \mathrm{A}y^5+\mathrm{B}x^2y^3+\mathrm{C}y^3+\mathrm{D}x^2y+\mathrm{E}x^2 \tag{25}$$

where A, B, C, D, E are constants. Then the plastic stress components can be obtained:

$$\left.\begin{aligned}\left(\sigma_x^p\right)_f &= \frac{\partial^2\Phi}{\partial y^2} = 20\mathrm{A}y^3+6\mathrm{B}x^2y+6\mathrm{C}y\\ \left(\sigma_y^p\right)_f &= \frac{\partial^2\Phi}{\partial x^2}-\gamma y = 2\mathrm{B}y^3+2\mathrm{D}y+2\mathrm{E}-\gamma y\\ \left(\tau_{xy}^p\right)_f &= -\frac{\partial^2\Phi}{\partial x\partial y} = -6\mathrm{B}xy^2-2\mathrm{D}x\end{aligned}\right\} \tag{26}$$

The bottom of plastic zone for roof is stress boundary condition:

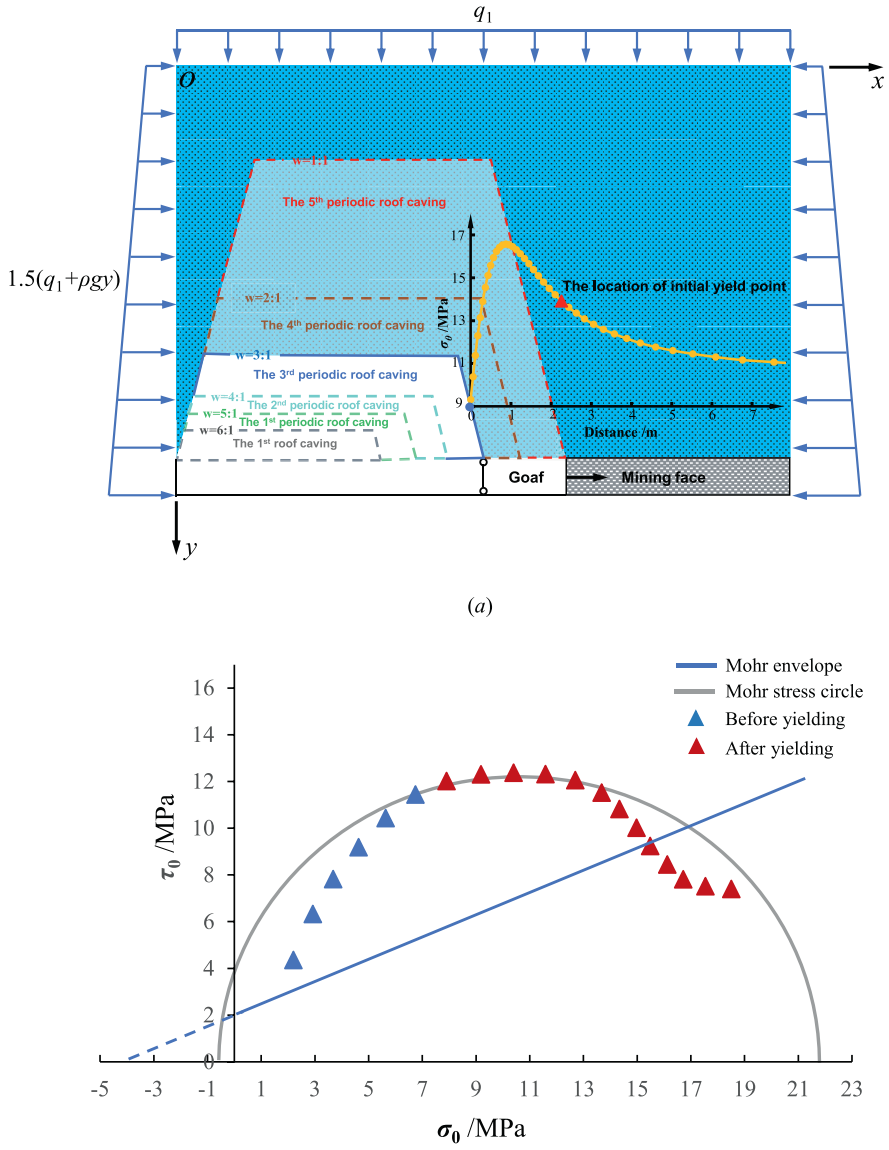

Fig. 6. The variation of τ_0 with σ_0 at the initial yield point in the complex functions model of the overburden roof when $k = 1.5$. (a) The location of initial yield point of overburden roof when $k = 1.5$; (b) The variation of τ_0 with σ_0 at the initial yield point.

$$\left.\begin{aligned}\left(\sigma_y^p\right)_f|_{y=\frac{h}{2}} &= 0\\ \left(\tau_{xy}^p\right)_f|_{y=\frac{h}{2}} &= 0\end{aligned}\right\} \tag{27}$$

Then, $D = -\frac{3}{4}Bh^2$, $E = \frac{1}{4}Bh^3 + \frac{1}{4}\gamma h$ can be calculated by Eqs. (26) and (27). When the plastic zone extends to the roof top:

$$\left.\begin{aligned}\left(\sigma_y^p\right)_f|_{y=\frac{h}{2}} &= -(q_2 + 0.5\gamma h)\\ \left(\tau_{xy}^p\right)_f|_{y=\frac{h}{2}} &= 0\end{aligned}\right\} \tag{28}$$

and $B = -\frac{q_2+0.5\gamma h}{h^3}$ can be calculated by Eqs. (26) and (28). In the plastic stage, strain-displacement relationship is listed:

$$\left.\begin{aligned}\left(\varepsilon_x^p\right)_f &= \frac{\partial\left(u^p\right)_f}{\partial x}\\ \left(\varepsilon_y^p\right)_f &= \frac{\partial\left(v^p\right)_f}{\partial y}\\ \left(\gamma_{xy}^p\right)_f &= \frac{\partial\left(v^p\right)_f}{\partial x} + \frac{\partial\left(u^p\right)_f}{\partial y}\end{aligned}\right\} \tag{29}$$

where $\left.\begin{aligned}\sigma_0 &= \frac{1}{2}(\sigma_x+\sigma_y) - \sqrt{(\sigma_x-\sigma_y)^2 + 4(\tau_{xy})^2}\sin\varphi\\ \tau_0 &= \sqrt{(\sigma_x-\sigma_y)^2 + 4(\tau_{xy})^2}\cos\varphi\end{aligned}\right\}$, $\left.\begin{aligned}\sigma_0 &= \frac{1}{2}(\sigma_x+\sigma_y) - \sqrt{(\sigma_x-\sigma_y)^2 + 4(\tau_{xy})^2}\sin\varphi\\ \tau_0 &= \sqrt{(\sigma_x-\sigma_y)^2 + 4(\tau_{xy})^2}\cos\varphi\end{aligned}\right\}$ and $\left.\begin{aligned}\sigma_0 &= \frac{1}{2}(\sigma_x+\sigma_y) - \sqrt{(\sigma_x-\sigma_y)^2 + 4(\tau_{xy})^2}\sin\varphi\\ \tau_0 &= \sqrt{(\sigma_x-\sigma_y)^2 + 4(\tau_{xy})^2}\cos\varphi\end{aligned}\right\}$ represent the normal strain components along the x and y axes and the shear strain component

within the plastic zone of the statically indeterminate beam; $\left.\begin{aligned}\sigma_0 &= \frac{1}{2}(\sigma_x+\sigma_y)-\sqrt{(\sigma_x-\sigma_y)^2+4(\tau_{xy})^2}\sin\varphi \\ \tau_0 &= \sqrt{(\sigma_x-\sigma_y)^2+4(\tau_{xy})^2}\cos\varphi\end{aligned}\right\}$, $\left.\begin{aligned}\sigma_0 &= \frac{1}{2}(\sigma_x+\sigma_y)-\sqrt{(\sigma_x-\sigma_y)^2+4(\tau_{xy})^2}\sin\varphi \\ \tau_0 &= \sqrt{(\sigma_x-\sigma_y)^2+4(\tau_{xy})^2}\cos\varphi\end{aligned}\right\}$ correspond to the displacement components along the x and y axes, respectively.

Eq. (30) can be deduced from Eq. (29):

$$\frac{\partial^2\left(\varepsilon_x^p\right)_f}{\partial y^2}+\frac{\partial^2\left(\varepsilon_y^p\right)_f}{\partial x^2}=\frac{\partial^2\left(\gamma_{xy}^p\right)_f}{\partial x\partial y} \tag{30}$$

and the total deformation theory of plastic mechanics is listed as Eq. (31):

$$S_{ij}=\frac{2\sigma_i}{3\varepsilon_i}e_{ij}=\begin{cases}\left(\sigma_x^p\right)_f-\sigma_m=2G'\left(\left(\varepsilon_x^p\right)_f-\varepsilon_m\right)\\ \left(\sigma_y^p\right)_f-\sigma_m=2G'\left(\left(\varepsilon_y^p\right)_f-\varepsilon_m\right)\\ \left(\sigma_z^p\right)_f-\sigma_m=2G'\left(\left(\varepsilon_z^p\right)_f-\varepsilon_m\right)\\ \left(\tau_{xy}^p\right)_f=G'\left(\gamma_{xy}^p\right)_f\end{cases} \tag{31}$$

where S_{ij}, e_{ij} represent stress deviator components and strain deviator components, respectively; σ_i, ε_i represent stress intensity and strain intensity, respectively; σ_m, ε_m represent mean stress and mean strain, respectively; $\left.\begin{aligned}\sigma_0 &= \frac{1}{2}(\sigma_x+\sigma_y)-\sqrt{(\sigma_x-\sigma_y)^2+4(\tau_{xy})^2}\sin\varphi \\ \tau_0 &= \sqrt{(\sigma_x-\sigma_y)^2+4(\tau_{xy})^2}\cos\varphi\end{aligned}\right\}$ and $\left.\begin{aligned}\sigma_0 &= \frac{1}{2}(\sigma_x+\sigma_y)-\sqrt{(\sigma_x-\sigma_y)^2+4(\tau_{xy})^2}\sin\varphi \\ \tau_0 &= \sqrt{(\sigma_x-\sigma_y)^2+4(\tau_{xy})^2}\cos\varphi\end{aligned}\right\}$ represent the normal stress and normal strain components along the z axe within the plastic zone of the statically indeterminate beam, respectively. G' is a parameter expressed by stress intensity and strain intensity, $G'=\frac{\sigma_i}{3\varepsilon_i}$. It is assumed that Poisson's ratio can be 0.5 in the plane strain problem, $\varepsilon_z=0$, $(\sigma_z^p)_f=0.5((\sigma_x^p)_f+(\sigma_y^p)_f)$, and mean stress is listed as Eq. (32):

$$\sigma_m=0.5\left(\left(\sigma_x^p\right)_f+\left(\sigma_y^p\right)_f\right) \tag{32}$$

and A = −0.2B can be calculated by Eqs. (24), (26) and (30)–(32).

The boundary point ($x=0$; $y=0.5h$) first enters plastic state according to the deformation of roof, and the stress of this point should satisfy the Mohr-Coulomb yield condition. By Eq. (21) and Eq. (26), $C=\frac{Bk_1h^3-2m_1}{6k_1h}$ can be calculated, where k_1 is a constant, $k_1=\frac{1+\sin\varphi}{1-\sin\varphi}$.

The plastic stress components of the overburden roof during the first caving can be clearly presented by substituting the value of A, B, C, D and E into Eq. (26):

$$\left.\begin{aligned}\left(\sigma_x^p\right)_f &= \frac{4q_2+4\gamma h}{h^3}y^3-\frac{6q_2+6\gamma h}{h^3}x^2y-\frac{q_2k_1+\gamma hk_1+2m_1}{hk_1}y\\ \left(\sigma_y^p\right)_f &= -\frac{2q_2+2\gamma h}{h^3}y^3+\frac{3q_2+\gamma h}{2h}y-\frac{q_2}{2}-\gamma y\\ \left(\tau_{xy}^p\right)_f &= \frac{6q_2+6\gamma h}{h^3}xy^2-\frac{3q_2+\gamma h}{2h}x\end{aligned}\right\} \tag{33}$$

where the x direction normal stress, y direction normal stress and shear stress of statically indeterminate beam of the overburden roof during the first caving in the plastic stage are $(\sigma_x^p)_f$, $(\sigma_y^p)_f$, $(\tau_{xy}^p)_f$.

With the advance of the mining face, there are both elastic and plastic zones in the roof when the roof enters the state of elastic-plastic

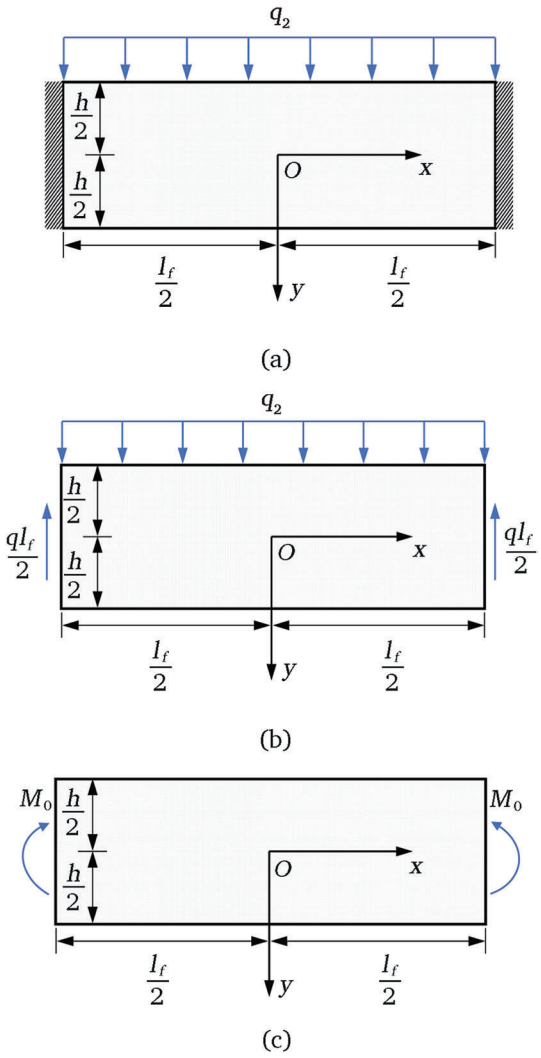

Fig. 7. Decomposition diagram of the mechanical model for the first caving of the overburden roof. (a) The statically indeterminate beam with two fixed boundaries; (b) The statically determinate beam with vertical reaction forces at both boundaries; (c) The statically determinate beam with two bending moments at both boundaries.

deformation. It is assumed that the functional expression of the boundary line between the elastic zone and the plastic zone is $y=y_s(x)(-0.5h\le y_s(x)\le 0.5h)$.

It can be obtained from the stress continuity condition on the boundary line:

$$\left(\sigma_x^e\right)_f=\left(\sigma_x^p\right)_f \tag{34}$$

the boundary line can be calculated by Eqs. (21), (32) and (34):

$$\frac{y_s^2}{\frac{A_3}{A_1}}-\frac{x^2}{\frac{A_3}{A_2}}=1 \tag{35}$$

where $A_1=\frac{2\gamma}{h^2}$, $A_2=\frac{3\gamma}{h^2}$, $A_3=-\frac{2q_2+\gamma h}{4h^3}l_f^2+\frac{2q_2}{5h}+\frac{7\gamma}{10}+\frac{2m_1}{hk_1}$.

It can be seen from Eq. (35) that the boundary line between the elastic zone and the plastic zone is a hyperbola curve. Combined with the deformation characteristics of the roof, the outer area above the boundary line is the elastic zone and the inner area below the boundary line is the plastic zone.

Due to the confinement effect of the elastic zone on plastic deformation, localized yielding within the plastic zone does not necessarily lead to catastrophic roof collapse. From the perspective of stress balance

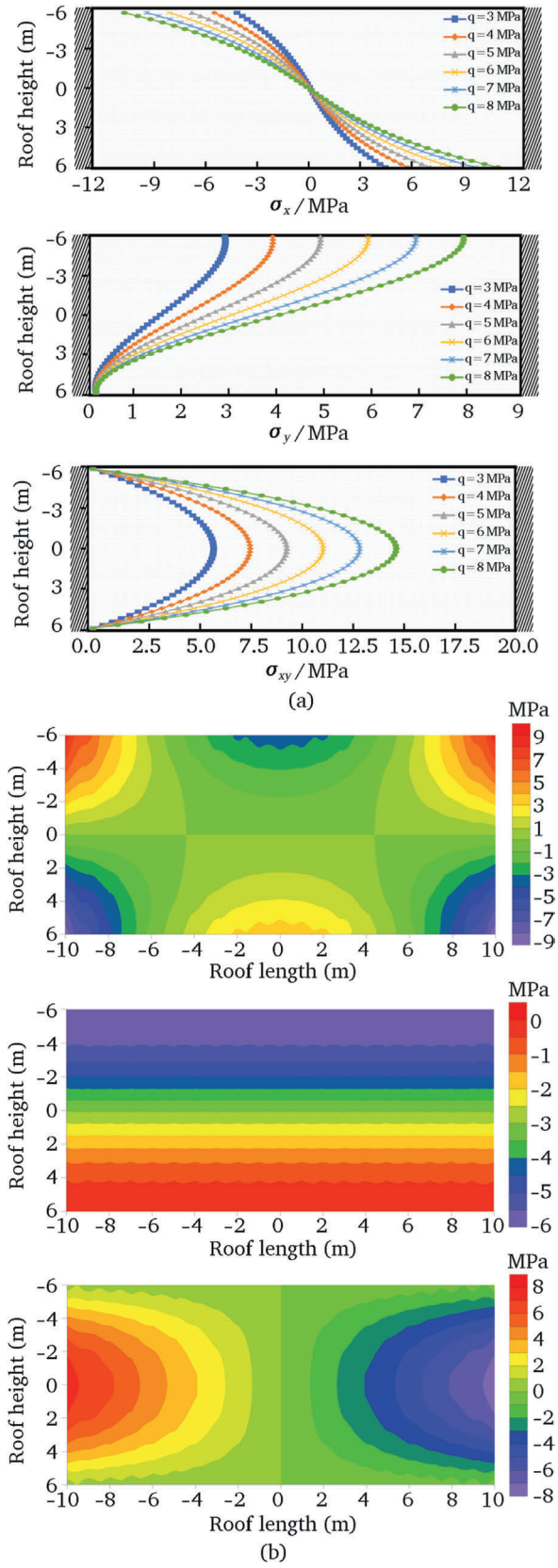

Fig. 8. The stress components distribution in the elastic deformation stage of the immediate roof during the first caving. (*a*) The distribution of stress in the overburden roof under different loadings; (*b*) The two-dimensional contour map of σ_x, σ_y, τ_{xy} in the overburden roof during the first caving.

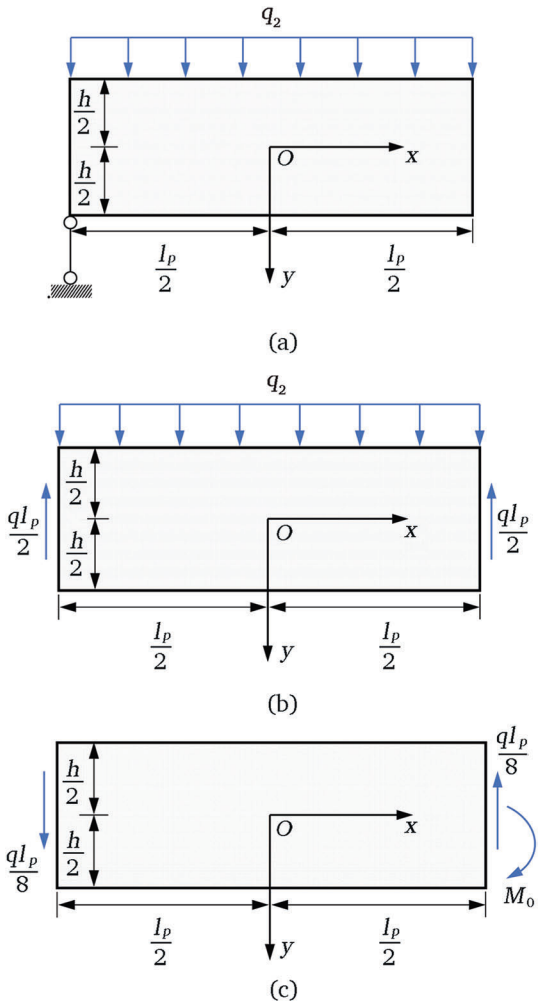

Fig. 9. Decomposition diagram of the mechanical model for the periodic caving of the overburden roof. (a) The statically indeterminate beam with a fixed boundary and a hinged boundary; (b) The statically determinate beam with vertical reaction forces at both boundaries; (c) The statically determinate beam with a bending moment and a vertical reaction force.

at the boundary line of overburden roof caving, the discriminant condition of overburden roof caving is proposed: the overhang length of overburden roof gradually increases and the scope of the plastic zone slowly expands with mining face advancement, when the total tensile stress of the boundary line between the elastic zone and the plastic zone is less than the gravity of the plastic zone, the rock strata in the plastic zone will occur caving.

The boundary line is a curve and mechanical analysis is performed on a triangular micro-element at any point on the boundary line, as shown in Fig. 2, θ is the angle between the boundary of the caving space and the *x*-axis. It can be obtained that the normal stress and shear stress on any inclined plane passing through the point on the boundary line are expressed:

$$\left.\begin{aligned}(\sigma_n)_f &= l_n^{\,2}\left(\sigma_x^p\right)_f + m_n^{\,2}\left(\sigma_y^p\right)_f + 2l_n m_n\left(\tau_{xy}^p\right)_f \\ (\tau_n)_f &= l_n m_n\left(\left(\sigma_y^p\right)_f - \left(\sigma_x^p\right)_f\right) + \left(l_n^{\,2} - m_n^{\,2}\right)\left(\tau_{xy}^p\right)_f\end{aligned}\right\} \tag{36}$$

where $(\sigma_n)_f$, $(\tau_n)_f$ represent the normal stress and shear stress on any inclined plane passing through the point, respectively; l_n, m_n represent the direction cosine of the angle between *x* axis, *y* axis and the normal line of the inclined plane, respectively. And the limit equilibrium conditions for the plastic zone are listed:

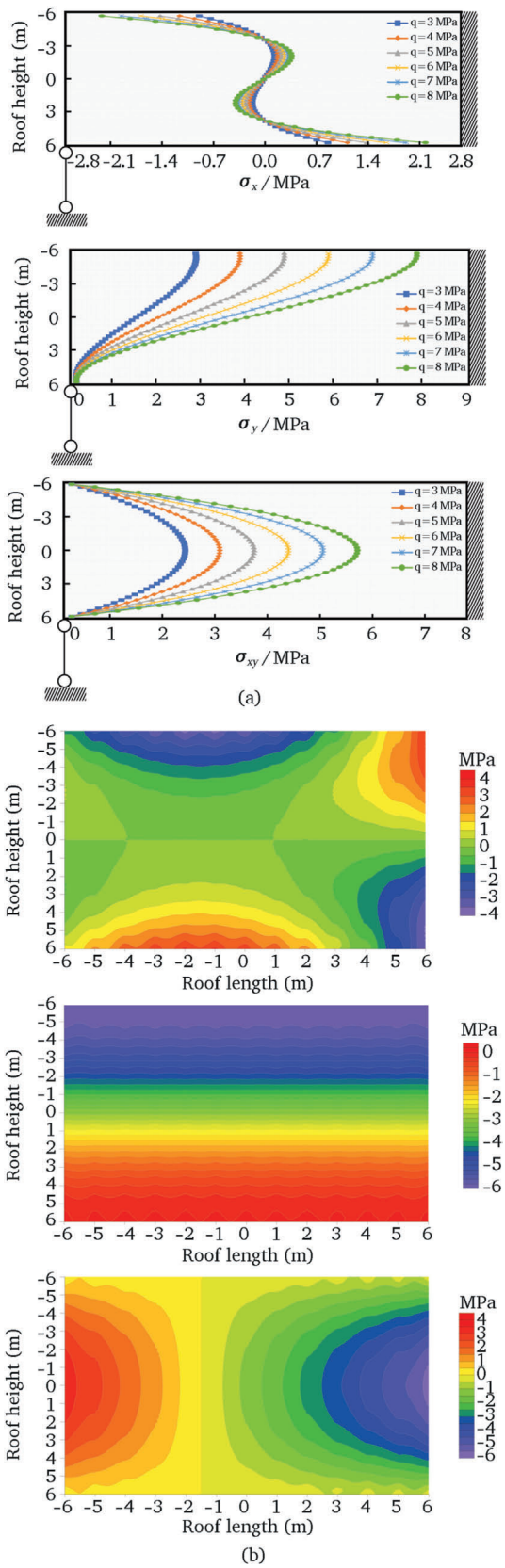

Fig. 10. The stress components distribution in the elastic deformation stage of the immediate roof during the periodic caving. (a) The distribution of stress in the overburden roof under different loadings; (b) The two-dimensional contour map of σ_x, σ_y, τ_{xy} in the overburden roof during the periodic caving.

$$\left.\begin{aligned}\Sigma F_x &= \Sigma l_n(\sigma_n)_f dL_0 - \Sigma m_n(\tau_n)_f dL_0 = 0\\ \Sigma F_y &= \Sigma m_n(\sigma_n)_f dL_0 + \Sigma l_n(\tau_n)_f dL_0 - \Sigma\gamma dS_0 = 0\end{aligned}\right\} \tag{37}$$

where F_x, F_y are the resultant force in x direction and y direction on the boundary line, respectively. L_0, S_0 are the length of the boundary line and the area of the plastic zone, respectively. The calculation for the length L_0 of the boundary line is listed:

$$L_0 = 2\int_0^{\sqrt{\frac{h^2}{4}\frac{A_1}{A_2}-\frac{A_3}{A_2}}} \sqrt{1+\frac{A_2{}^2x^2}{A_1A_3+A_1A_2x^2}}\,\mathrm{d}x \tag{38}$$

and the calculation for the area S_0 of the plastic zone is listed:

$$S_0 = h\sqrt{\frac{h^2}{4}\frac{A_1}{A_2}-\frac{A_3}{A_2}} + 2\int_0^{\sqrt{\frac{h^2}{4}\frac{A_1}{A_2}-\frac{A_3}{A_2}}} \sqrt{\frac{A_2}{A_1}\left(\frac{A_3}{A_2}+x^2\right)}\,\mathrm{d}x \tag{39}$$

In addition, by combining Eqs. (37)–(39), the limit equilibrium condition in the y direction can be further transformed into:

$$\int_{b_f}^{a_f}(\sigma_n)_f\mathrm{d}x + \int_{-\frac{h}{2}}^{c_f}(\tau_n)_f\mathrm{d}y = \gamma S_0 \tag{40}$$

Where $a_f = \sqrt{\frac{A_1}{A_2}\frac{h^2}{4}-\frac{A_3}{A_2}}$, $b_f = -\sqrt{\frac{A_1}{A_2}\frac{h^2}{4}-\frac{A_3}{A_2}}$, $c_f = -\sqrt{\frac{A_2}{A_1}x^2+\frac{A_3}{A_1}}$.

By simultaneously solving Eqs. (32), (35), (37), (39) and (40), when the first caving of overburden roof occurs in the plastic zone, the critical length of overburden roof can be obtained.

In order to analyze the stress distribution characteristics of the first caving region in the overburden roof during the elastic deformation stage in the advancement process of the mining face, the geological conditions of 21221 mining face of Qianqiu coal mine are adopted as the engineering background. The length and height of overburden roof are set as 20 m, 12 m, respectively. And the overburden roof is mudstone with an average thickness of 24 m. The parameter q_2 is set as 6 MPa from the gravity of rock strata above the roof.

Fig. 8 presents the stress distribution results for the overburden roof in the elastic deformation stage during the first caving. In this figure, the distribution of stress in the overburden roof under different loadings is shown by several curves in the cross section of roof. With the increase of the loading on the top boundary of the roof, there is an increasing phenomenon of σ_x, σ_y, τ_{xy} at the same height of roof, but the increase amplitude of stress components is not consistent along the roof height. In Fig. 8, the two-dimensional contour map of σ_x, σ_y, τ_{xy} in the overburden roof during the first caving are also presented. The σ_x and τ_{xy} show a symmetrical distribution with respect to the central longitudinal axis of the roof, and the σ_y shows gradual nonlinear increase along the roof height.

3.3. Stress calculation in overburden roof during the periodic caving

Following the first caving of the overburden roof, the periodic caving will occur. During this stage, the mechanical model of the overburden roof during the periodic caving can be considered as a statically indeterminate beam with one fixed boundary and one hinged boundary based on the complex functions model, as illustrated in Fig. 9a. The superposition principle is then applied to transform this statically indeterminate structure into the superposition of two statically determinate beams as illustrated in (Fig. 9b and c). The roof overhang length is l_p corresponding to the advancement distance of the mining face.

Similar to the first caving, the overburden roof undergoes elastic deformation prior to periodic caving. The stress components in the elastic stage of the overburden roof during the periodic caving can be obtained by elastic mechanics theory (Xu, 2016):

$$\left.\begin{aligned}
\left(\sigma_x^e\right)_p &= \frac{(4q_2+2\gamma h)y^3}{h^3} - \frac{(6q_2+3\gamma h)x^2 y}{h^3} - \frac{3(q_2+0.5\gamma h)l_p xy}{2h^3} + \frac{3(q_2+0.5\gamma h)y}{h}\left(\frac{l_p^2}{4h^2}-\frac{1}{5}\right)\\
\left(\sigma_y^e\right)_p &= -\frac{(2q_2+\gamma h)}{h^3}y^3 + \frac{3}{2}\frac{(q_2+0.5\gamma h)}{h}y - \frac{(q_2+0.5\gamma h)}{2}\\
\left(\tau_{xy}^e\right)_p &= \frac{(6q_2+3\gamma h)}{h^3}xy^2 + \frac{3}{2}\frac{(q_2+0.5\gamma h)l_p}{2h^3}y^2 - \frac{3}{2}\frac{(q_2+0.5\gamma h)}{h}x - \frac{3}{8}\frac{(q_2+0.5\gamma h)l_p}{2h}
\end{aligned}\right\} \tag{41}$$

where the normal stress in x direction, normal stress in y direction, and the shear stress of statically indeterminate beam of the overburden roof during the elastic stage of periodic caving are $(\sigma_x^e)_p$, $(\sigma_y^e)_p$, $(\tau_{xy}^e)_p$.

As the mining face advances, the roof transitions from the elastic to plastic state. According to the deformation characteristics of statically indeterminate beam of the overburden roof during the periodic caving, the boundary point ($x = 0.5l_p$; $y = 0.5h$) in statically indeterminate beam first enters the plastic state. By substituting the stress obtained from Eq. (41) of the boundary point ($x = 0.5l_p$; $y = 0.5h$) into Eq. (19), the critical length l_p of the roof can be listed as follows:

$$l_p = 2\sqrt{\left(-\frac{m_1}{3q_2+1.5pgh}+\frac{1}{15}\right)h^2} \tag{42}$$

When the roof enters the plastic state, the calculation method and derivation process of the plastic stress components of the overburden roof during the periodic caving are same as those used the first caving. However, it is worth pointing out that the boundary conditions are different between the two stages. The plastic stress components of the overburden roof during the periodic caving can be expressed as:

$$\left.\begin{aligned}
\left(\sigma_x^p\right)_p &= \frac{4q_2+4\gamma h}{h^3}y^3 - \frac{6q_2+6\gamma h}{h^3}x^2 y - \frac{(1+4k_1)(q_2+\gamma h)h^2 - 6k_1(q_2+\gamma h)l_p^2 + 8m_1h^2}{4h^3k_1}y\\
\left(\sigma_y^p\right)_p &= -\frac{2q_2+2\gamma h}{h^3}y^3 + \frac{3q_2+\gamma h}{2h}y - \frac{q_2}{2} - \gamma y\\
\left(\tau_{xy}^p\right)_p &= \frac{6q_2+6\gamma h}{h^3}xy^2 - \frac{3q_2+\gamma h}{2h}x
\end{aligned}\right\} \tag{43}$$

where the normal stress in x direction, normal stress in y direction, and shear stress of statically indeterminate beam of the overburden roof during the plastic stage of periodic caving are $(\sigma_x^p)_p$, $(\sigma_y^p)_p$, $(\tau_{xy}^p)_p$.

It is assumed that the boundary line between the elastic zone and the plastic zone is $y = h_s(x)(-0.5h \le h_s(x) \le 0.5h)$, it can be obtained from the stress continuity condition on the boundary line:

$$\left(\sigma_x^e\right)_p = \left(\sigma_x^p\right)_p \tag{44}$$

the boundary line can be calculated by Eqs. (41), (42) and (44):

$$\frac{A_4 h_s^2}{A_7} - \frac{A_5(x+A_6)^2}{A_7} = 1 \tag{45}$$

where $A_4 = \frac{4\gamma}{h^2}$, $A_5 = \frac{6\gamma}{h^2}$, $A_6 = -\frac{q_2 l_p}{8\gamma h}$, $A_7 = \frac{(1+4k)(q_2+\gamma h)h^2 - 6k(q_2+\gamma h){l_p}^2 + 8mh^2}{4h^3k} + A_8$, $A_8 = \frac{3{q_2}{l_p}^2}{4h^3} - \frac{3q_2}{5h} - \frac{3{q_2}^2{l_p}^2}{32\gamma h^4}$.

Eq. (45) reveals that the boundary line between the elastic zone and the plastic zone assumes a hyperbolic curve. It can be found that the boundary line between the elastic zone and the plastic zone show an

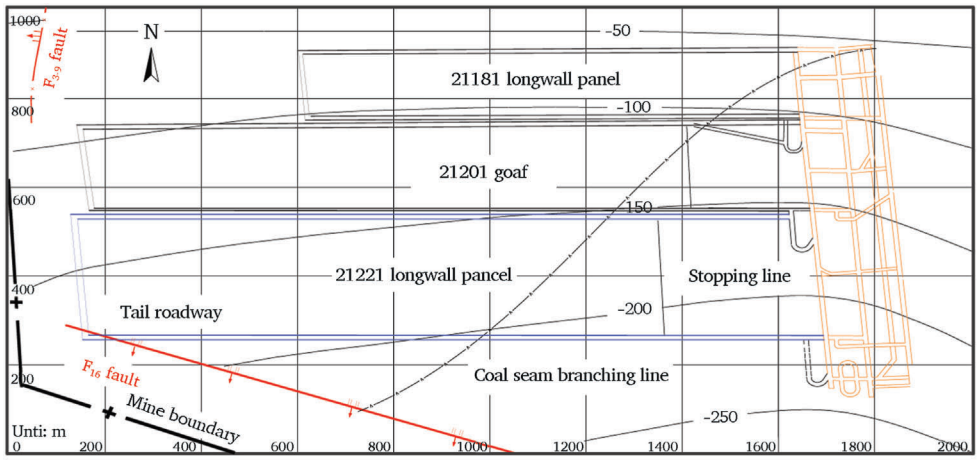

Rock type	Thickness (m)			Density (kg/m³)	UCS (MPa)
	Max.	Min.	Mean		
Conglomerate rock	580.50	96.35	550.00	2700	45
Mudstone	42.20	4.40	24.00	2170	30
Sandstone	27.00	0	10.00	2200	27
No.2 coal	37.48	5.59	9.60	1440	16
Siltstone	32.81	0.30	26.00	2600	30

Fig. 11. Mining layout and stratigraphic column of 21221 longwall panel.

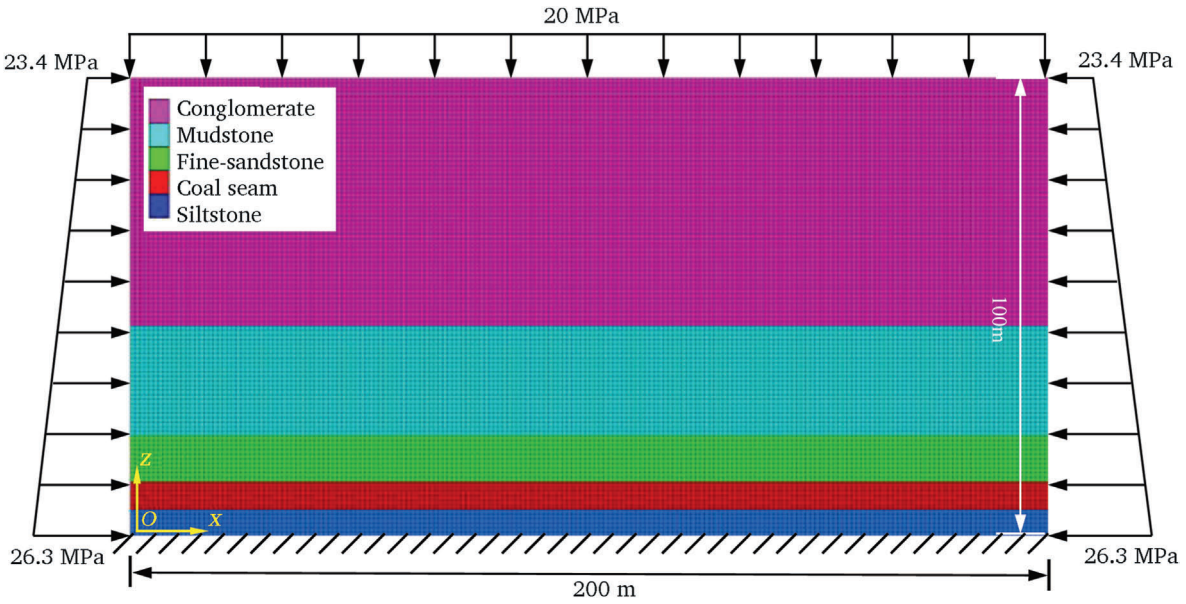

Fig. 12. Numerical model and the boundary conditions.

Table 1
Physical and mechanical parameters of rock strata.

Rock type	Bulk modulus (GPa)	Shear modulus (GPa)	Cohesion (MPa)	Friction angle (°)	Tensile Strength (MPa)	Density (kg/m^3)
Siltstone	9.8	5.6	8.9	42	3.6	2660
Coal seam	5.0	1.5	2.1	35	0.9	1430
Sandstone	6.0	2.0	3.3	33	1.8	2630
Mudstone	5.6	2.6	3.1	36	1.5	2560
Conglomerate	4.0	1.4	3.0	30	1.4	2780

obvious difference between the mechanical model of first caving of the overburden roof and that during periodic caving.

According to the previous analysis of the discriminant conditions for overburden roof caving from the perspective of stress balance at the boundary line, when the total tensile stress of the boundary line between the elastic zone and the plastic zone is less than the gravity of the plastic zone, the rock strata in the plastic zone will occur caving. The boundary line is a curve and mechanical analysis is conducted on a triangular micro-element at any point on the boundary line, as shown in Fig. 2. During the periodic caving of the overburden roof, it can be obtained that the normal stress and shear stress on any inclined plane passing through the point on the boundary line are expressed:

$$\left.\begin{aligned}(\sigma_n)_p &= l_n{}^2\left(\sigma_x^p\right)_p + m_n{}^2\left(\sigma_y^p\right)_p + 2l_n m_n\left(\tau_{xy}^p\right)_p \\ (\tau_n)_p &= l_n m_n\left(\left(\sigma_y^p\right)_p - \left(\sigma_x^p\right)_p\right) + \left(l_n{}^2 - m_n{}^2\right)\left(\tau_{xy}^p\right)_p\end{aligned}\right\} \tag{46}$$

where $(\sigma_n)_p$, $(\tau_n)_p$ represent the normal stress and shear stress on any inclined plane passing through the point, respectively. And the limit equilibrium conditions for the plastic zone are listed:

$$\left.\begin{aligned}\Sigma F_x &= \Sigma l_n(\sigma_n)_p dL_1 - \Sigma m_n(\tau_n)_p dL_1 = 0 \\ \Sigma F_y &= \Sigma m_n(\sigma_n)_p dL_1 + \Sigma l_n(\tau_n)_p dL_1 - \Sigma\gamma dS_1 = 0\end{aligned}\right\} \tag{47}$$

where L_1, S_1 are the length of the boundary line and the area of the plastic zone, respectively. The calculation for the length L_1 of the boundary line is listed:

$$dL_1 = \frac{dx}{m_n} \tag{48}$$

and the calculation for the area S_1 of the plastic zone is listed:

$$S_1 = L_s\frac{h}{2} - \int_{b_p}^{a_p}|k_s|dx \tag{49}$$

where $L_s = -\sqrt{\frac{h^2A_4}{4A_5} - \frac{A_7}{A_5}}$, $a_p = -A_6 + \sqrt{\frac{h^2A_4}{4A_5} - \frac{A_7}{A_5}}$, $b_p = -A_6 - \sqrt{\frac{h^2A_4}{4A_5} - \frac{A_7}{A_5}}$, $k_s = -\sqrt{\frac{A_3}{A_1} + \frac{A_2}{A_1}(x + A_6)^2}$, $l_n = -\frac{k_s'}{\sqrt{1+(k_s')^2}}$, $m_n = \frac{1}{\sqrt{1+(k_s')^2}}$.

In addition, by combining Eqs. (47)–(49), the limit equilibrium condition in the y direction can be further transformed into:

$$\int_{b_p}^{a_p}\left((\sigma_n)_p - k_s'(\tau_n)_p\right)\mathrm{d}x = \rho g h\frac{L_S}{2} - \rho g\int_{b_p}^{a_p}(|k_s|)\mathrm{d}x \tag{50}$$

By simultaneously solving Eqs. (42), (45), (46), (49) and (50), the critical overhang length of overburden roof when periodic caving occurs in the plastic zone can be obtained.

Based on the geological parameters provided above for the 21221

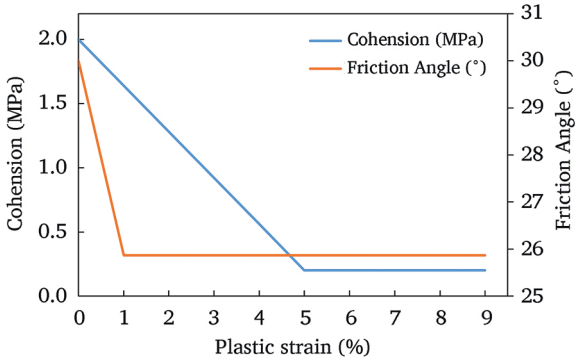

Fig. 13. Variation of cohesion and friction angle with plastic strain.

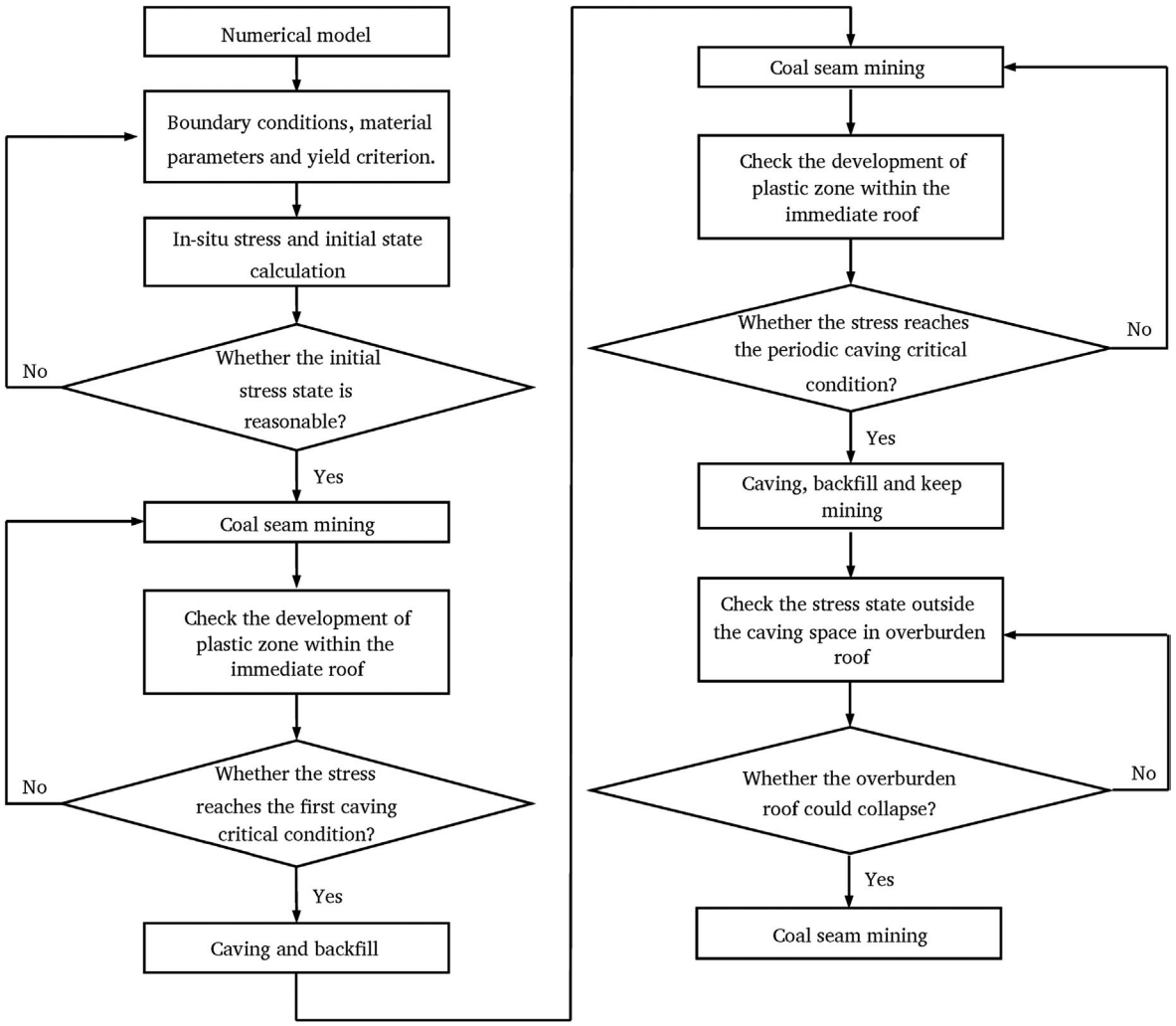

Fig. 14. Numerical simulation process and overburden roof caving identification.

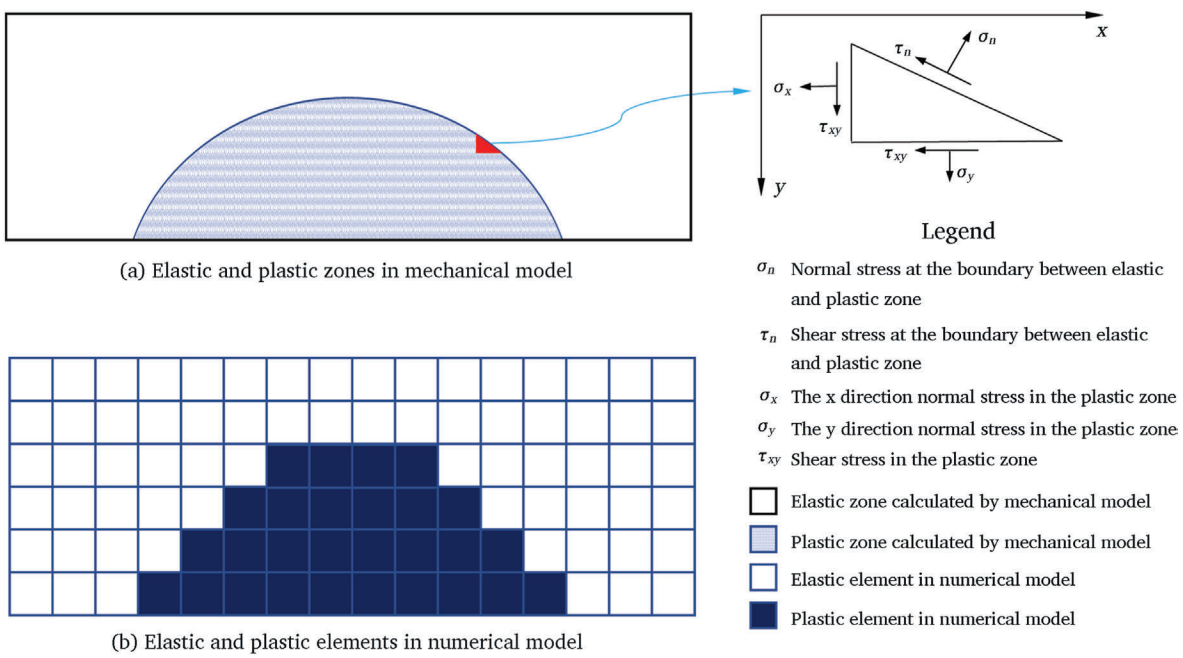

(a) Elastic and plastic zones in mechanical model

(b) Elastic and plastic elements in numerical model

Fig. 15. Identification of overburden roof caving in the numerical simulation. (a) Elastic and plastic zones in mechanical model; (b) Elastic and plastic elements in numerical model.

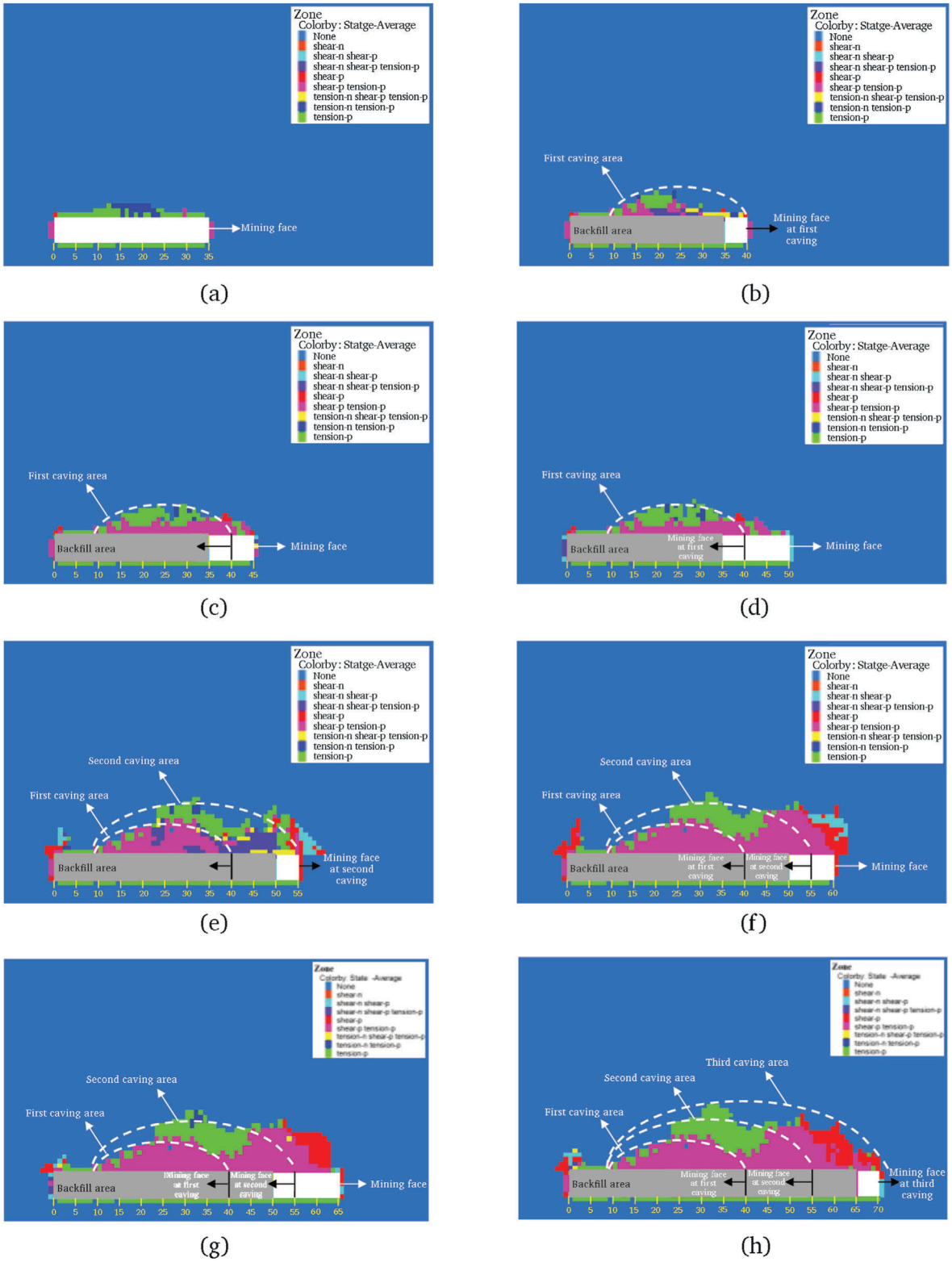

Fig. 16. Distribution of the plastic zone in the overburden roof and roof caving simulation results during coal seam mining. (a) Advancement distance 35 m; (b) Advancement distance 40 m; (c) Advancement distance 45 m; (d) Advancement distance 50 m; (e) Advancement distance 55 m; (f) Advancement distance 60 m; (g) Advancement distance 65 m; (h) Advancement distance 70 m.

mining face of Qianqiu mine, the stress distribution characteristics in the elastic deformation stage of the roof periodic caving are analyzed, as shown Fig. 10. It should be noted that the roof length of the periodic caving mechanical model is set as 12 m. The σ_x, σ_y, τ_{xy} in the overburden roof during periodic caving in the elastic stage under different loadings are presented by several curves in the cross section of roof. From the lower end to the upper end of the roof, the stress σ_x gradually transforms from tensile stress to compressive stress, and σ_y always appears as compressive stress and shows nonlinear increase, and τ_{xy} gradually increases to the peak value and then decreases to 0. In Fig. 10, two-

Table 2
Parameters of materials in physical model.

Rock strata	Prototype rock			Similarity materials		
	UCS (MPa)	Density (kg/m^3)	Thickness (m)	UCS (MPa)	Density (kg/m^3)	Thickness (cm)
Conglomerate	44.8	2700	550	0.28	1687	51
Mudstone	30.4	2170	24	0.19	1356	24
Sandstone	27.2	2200	10	0.17	1375	6
Coal seam	16.0	1440	9.6	0.10	900	6
Siltstone	30.4	2600	26	0.19	1625	13

Table 3
The weight of similar materials in physical model.

Rock strata	Layer height (cm)	Weight ratio	Fine sand (kg)	Gypsum (kg)	Lime (kg)	Water (kg)
Conglomerate	2	6.0:0.5:0.5:0.7	7.20	0.60	0.60	0.80
Mudstone	2	7.0:0.4:0.6:0.8	7.35	0.42	0.63	0.82
Sandstone	2	7.0:0.5:0.5:0.8	7.35	0.52	0.52	0.82
Coal seam	2	8.0:0.5:0.5:0.8	7.46	0.47	0.47	0.83
Siltstone	2	7:0.4:0.6:0.8	7.35	0.42	0.63	0.82

dimensional contours of σ_x, σ_y, τ_{xy} in the overburden roof during periodic caving are also presented. The distribution of σ_x and τ_{xy} are asymmetric along the roof length, due to the constraints on the left and right sides of the mechanical model of the overburden roof during periodic caving are not the same, and the σ_y shows symmetrically distributed along the roof length with respect to the central vertical axis of the roof.

4. Numerical simulation of overburden roof caving

4.1. Geological background

The geological conditions of 21221 mining face of Qianqiu coal mine in Henan province, China are taken as the engineering background, FLAC^{3D} code is utilized to simulate the caving process of overburden roof during the coal seam mining.

The main productive coal seam in Qianqiu coal mine is No.2 coal seam which is tectonically segmented by F_{16} fault during its formation and development. 21221 mining face with the longwall mining method is a typical longwall panel. Fig. 11 presents the mining layout of 21221 longwall panel and the southern boundary of 21221 longwall panel is adjacent to F_{16} fault and its northern boundary is 21201 goaf. The floor of 21221 longwall panel is siltstone with average thickness of 26 m, the immediate roof is fine sandstone with average thickness of 10 m and the main roof is mudstone with an average thickness of 24 m, whereas overburden roof is conglomerate rock with average thickness of 550 m and uniaxial compressive strength (UCS) of 45 MPa. It is known that the typical stratigraphic characteristics of 21221 longwall panel is the

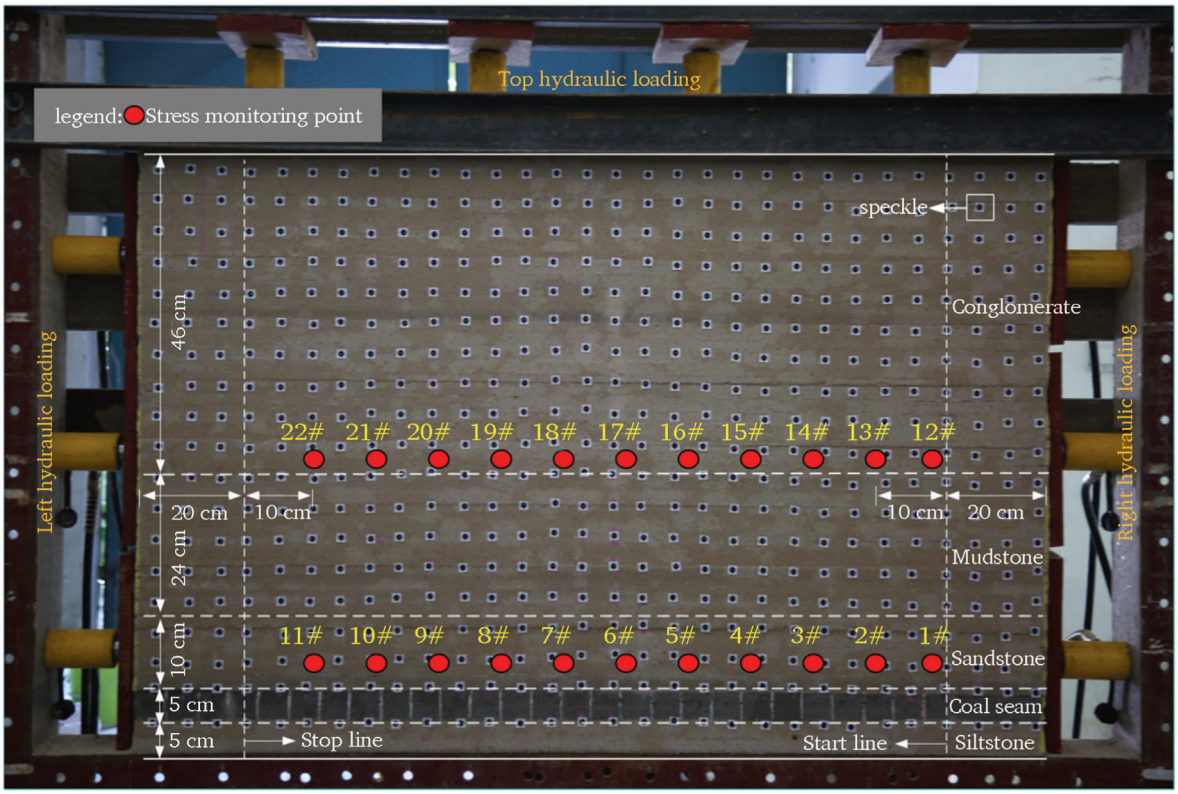

Fig. 17. The monitoring plan of stress and displacement in physical model.

occurrence of thick and hard conglomerate rock above coal seam.

4.2. Establishment of numerical model

The numerical model with geometrical dimension of 200 m × 100 m × 1 m is established, as shown in Fig. 12. The single element size is set as 1 m × 1 m × 1 m. The rock strata distribution from bottom to top in model is siltstone, coal seam, fine sandstone, mudstone and conglomerate. Table 1 shows the physical and mechanical parameters of rock strata in the numerical model. The thickness of the floor siltstone in the model is 26 m with good integrity, so a fixed displacement boundary is adopted to constrain both horizontal and vertical displacements, and vertical stress of 20 MPa is applied on the model top to simulate the overlying rock loading. Combined with the in-situ stress measurement data of 21221 mining face in Qianqiu coal mine, the lateral pressure coefficient is 1.17 and the horizontal stress is 23.4 MPa on left side and right side of model.

The model adopts strain softening constitutive model, the strain softening model describes the progressive degradation of material strength during plastic deformation, which used a modified Mohr-Coulomb criterion to consider the softening of cohesion and internal friction angle with equivalent plastic strain (ϵ^p), Fig. 13 shows the variation of cohesion and friction angle with plastic strain.

$$f = \sigma_1 - \sigma_3 N_\phi(\epsilon^p) + 2c(\epsilon^p)\sqrt{N_\phi(\epsilon^p)} \tag{51}$$

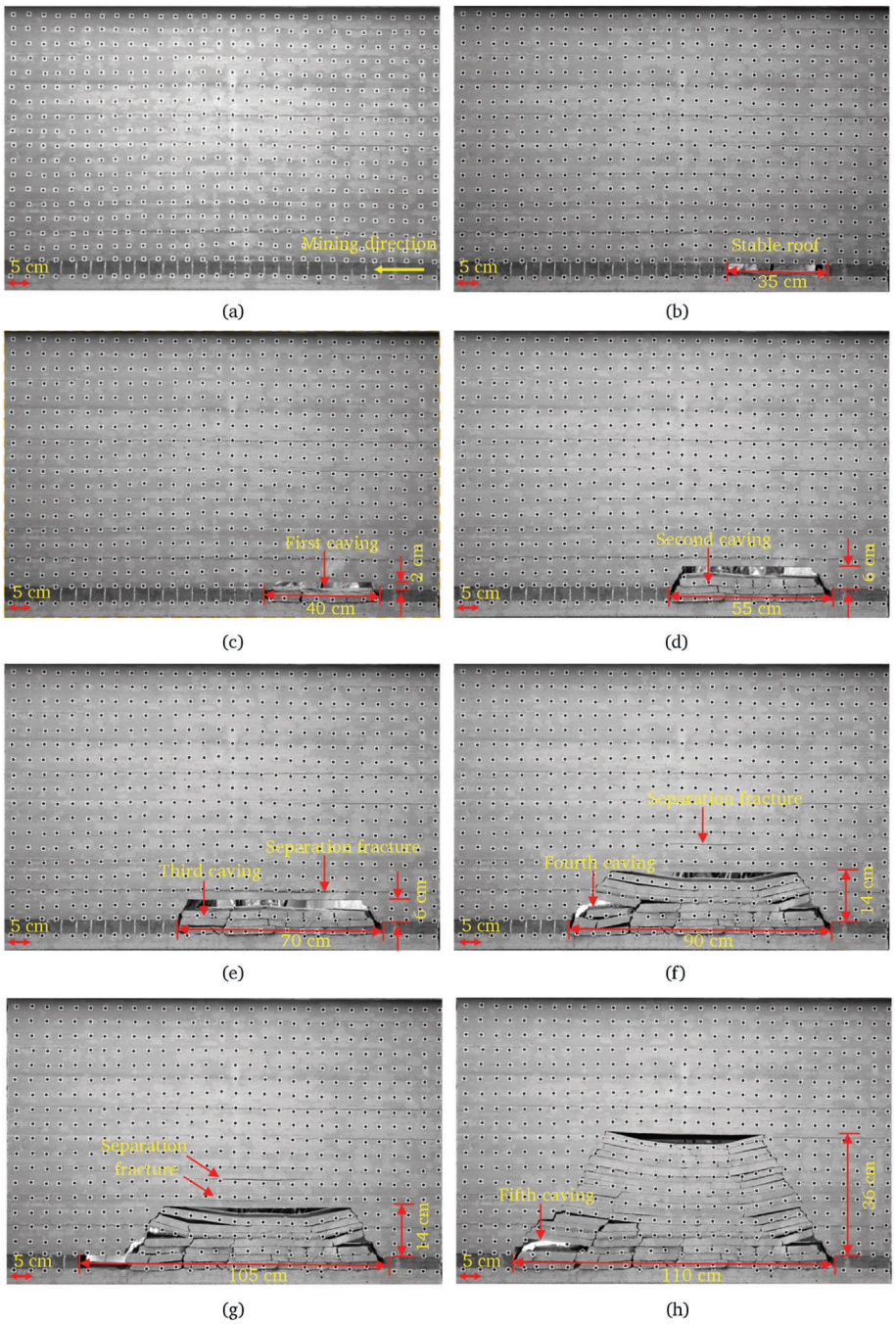

Fig. 18. Dynamic process of overburden roof caving during coal seam mining. (a) Mining 0 cm; (b) mining 35 cm; (c) mining 40 cm; (d) mining 55 cm; (e) mining 70 cm; (f) mining 90 cm; (g) mining 105 cm; (h) mining 110 cm.

where, $N_\phi(\epsilon^p) = \frac{1+\sin\phi(\epsilon^p)}{1-\sin\phi(\epsilon^p)}$, $c(\epsilon^p)$ is the cohesion degraded with plastic strain, $\phi(\epsilon^p)$ is the internal friction angle degraded with plastic strain.

Material parameters degrade with equivalent plastic strain:

$$c(\epsilon^p) = c \cdot f_c(\epsilon^p), \phi(\epsilon^p) = \phi \cdot f_\phi(\epsilon^p) \tag{52}$$

where $f_c(\epsilon^p)$ and $f_\phi(\epsilon^p)$ are softening functions, typically defined as piecewise linear or exponential decay:

$$f_c(\epsilon^p) = \begin{cases} 1 - \alpha_c \epsilon^p \\ e^{-\beta_c \epsilon^p} \end{cases} \tag{53}$$

Similar forms apply to $f_\phi(\epsilon^p)$.

The equivalent plastic strain is calculated based on the plastic shear strain:

$$\epsilon^p = \int \sqrt{\frac{2}{3}\dot{\epsilon}_{ij}^p \dot{\epsilon}_{ij}^p} \mathrm{d}t \tag{54}$$

where $\dot{\epsilon}_{ij}^p$ is the plastic strain rate tensor.

4.3. Criterion of overburden roof caving

Underground mining activities has a significant impact on the deformation and rock strata caving. As the mining face advances, the overburden roof will bend and sink. The identification algorithm of overburden roof caving, as depicted in Fig. 14, is designed in the numerical model. Initially, an accurate numerical model is constructed using the actual dimensions of overburden roof and coal seam.

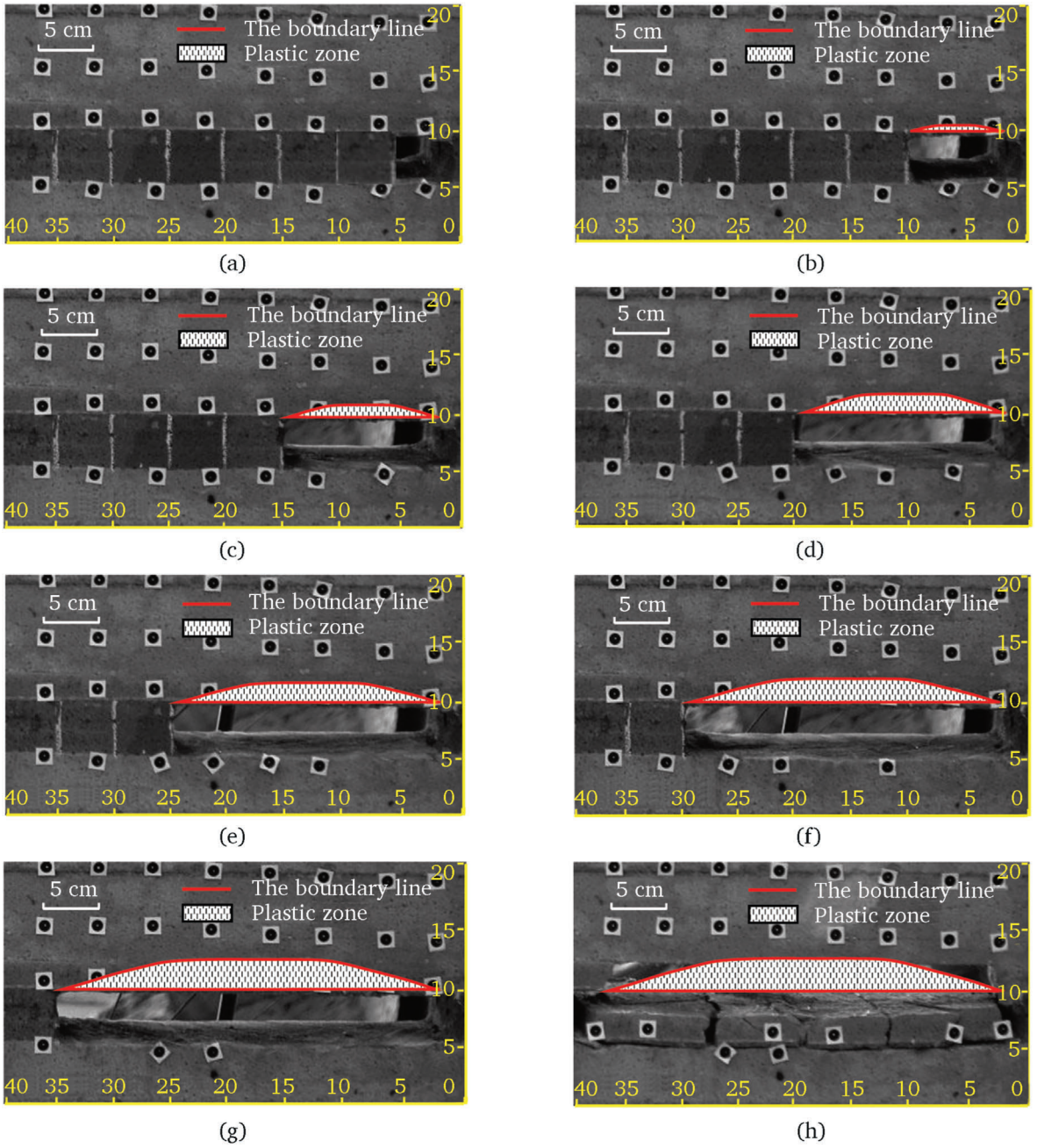

Fig. 19. Comparison of between mechanical model and physical model during the first caving of overburden roof (unit: cm). (a) Advancement distance 5 cm; (b) Advancement distance 10 cm; (c) Advancement distance 15 cm; (d) Advancement distance 20 cm; (e) Advancement distance 25 cm; (f) Advancement distance 30 cm; (g) Advancement distance 35 cm; (h) Advancement distance 40 cm.

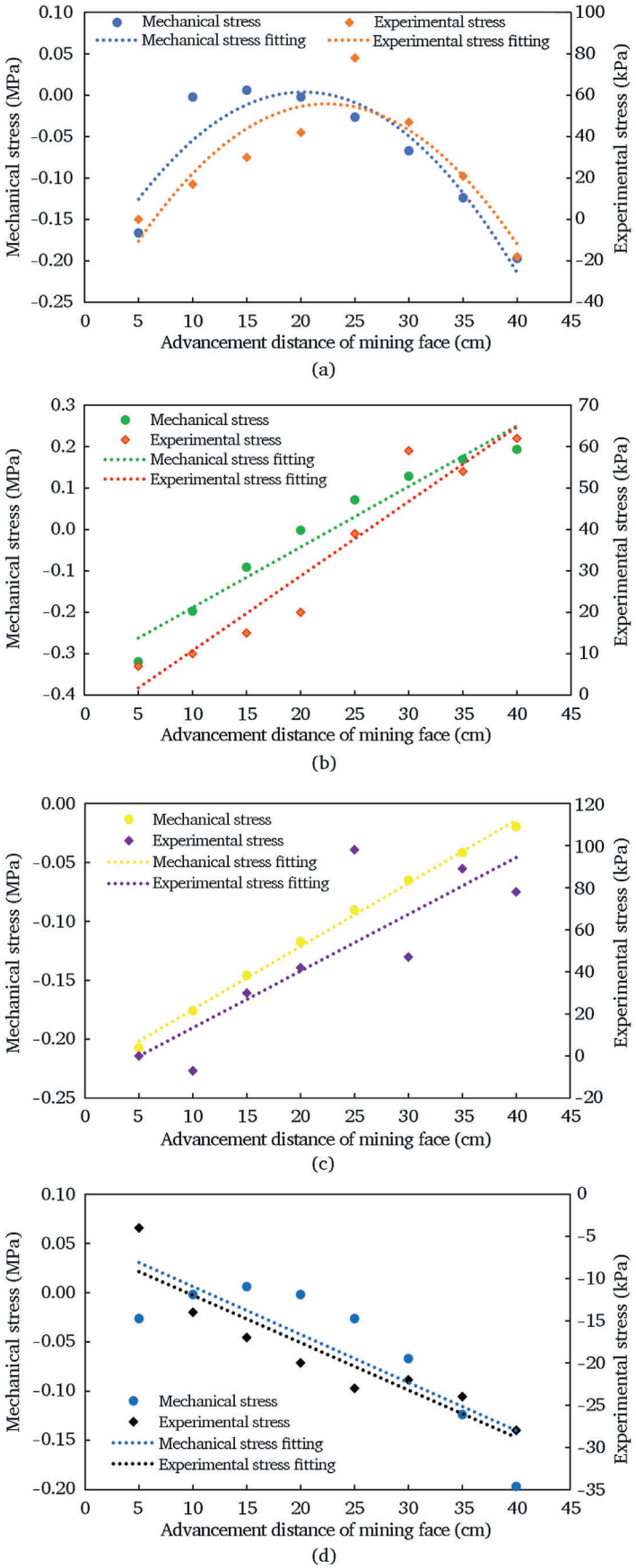

Fig. 20. Stress comparison between mechanical model and physical model during the first caving of overburden roof. (a) 1# monitoring point; (b) 2# monitoring point; (c) 3# monitoring point; (d) 5# monitoring point.

Subsequently, the basic properties of the numerical model are established, including boundary conditions, initial conditions, as well as the physical and mechanical parameters of rock strata and coal seam. The model continuously monitors the response of the in-site stress distribution and the maximum unbalance force. If the response results of the numerical model are deemed reasonable, the displacement and velocity of all elements and nodes are set to zero. However, if the response results are considered unreasonable, adjustments must be made to the basic properties of the numerical model. Additionally, the next step involves the advancement process of mining face, causing the rock strata to gradually transition into a plastic state. It is essential to identify the plastic elements of overburden roof above the goaf and group them together as the plastic zone. Furthermore, it is crucial to accurately identify and delineate the boundary elements of all plastic zones. This is accomplished by evaluating the state of the element directly above the plastic element, determining if it is in an elastic state. Through this assessment, the boundary elements of the entire plastic zone can be precisely identified and distinguished.

The above process involves iteratively scanning all the overburden roof elements to accurately identify the plastic zone elements and the boundary elements of the plastic zone. Subsequently, the total tensile stress of plastic zone boundary element and the total gravity of the plastic zone element are calculated. If the total stress state of the plastic zone boundary elements is found to be lower than the total gravity of the plastic zone elements, it indicates that an overburden roof caving will occur and backfilling of the goaf is carried out. It is important to emphasize that the calculation of the stress state and determination of whether the elements enter into the plastic state in the numerical model are completely based on the automatic calculations performed by the FLAC^{3D} code, and without any external intervention. The primary focus of this section is to locate the plastic elements within the numerical model and calculate the total stress state and total gravity, as shown in Fig. 15.

4.4. Numerical simulation results

In the numerical model, the blue elements represent the overburden roof in the elastic state, indicating that no caving is expected. On the other hand, the other colored elements represent areas of overburden roof that have the potential to cave during the coal seam mining, as shown in Fig. 16.

In the numerical model, as the mining face advances by 35 m, the overburden roof primarily experiences tensile failure. This leads to the expansion of the caving potential area not only horizontally along the advancing direction, but also vertically in an upward direction. The caving potential area exhibits a higher point in the middle and lower point on both sides, indicating an uneven distribution. This unevenness is attributed to the increased yielding of rock strata elements, which significantly raises the caving potential of overburden roof.

As the mining face advances by 40 m, the extent of plastic elements further expands. At this stage, the failure mechanism observed in the overburden roof includes both shear and tensile failure. Additionally, the maximum height of the caving potential area above the coal seam reaches 5 m. Based on the caving identification criterion in the numerical model, the overburden roof experiences its first caving at this point. As the mining face advances to 55 m and 70 m, the caving risk area of overburden roof expands significantly in both horizontal and vertical directions, and the overburden roof undergoes two successive periodic caving during this process.

The total advancement distance of the mining face is set to 70 m in the numerical model, and the overburden roof has experienced three times caving, including first caving and two subsequent periodic caving. It is observed that the advancement distance of the mining face in the numerical simulation aligns with the theoretical result of the critical length. This congruence confirms the reliability of both theoretical models and numerical simulations in characterizing the roof caving behavior during mining progression.

5. Physical model tests of overburden roof caving

5.1. Construction of physical model and monitoring scheme

To investigate the deformation and collapse characteristics of overburden strata during mining face advancement and the underlying mechanism of dynamic disasters, a physical simulation experiment was conducted based on the geological conditions of the 21221 mining face at Qianqiu coal mine. According to the similarity principle (He et al., 2009, 2022; Wang et al., 2020; Zhang et al., 2021), the similarity coefficient of geometry, density and strength were determined as 100, 1.6 and 160 respectively by comprehensively considering the properties of

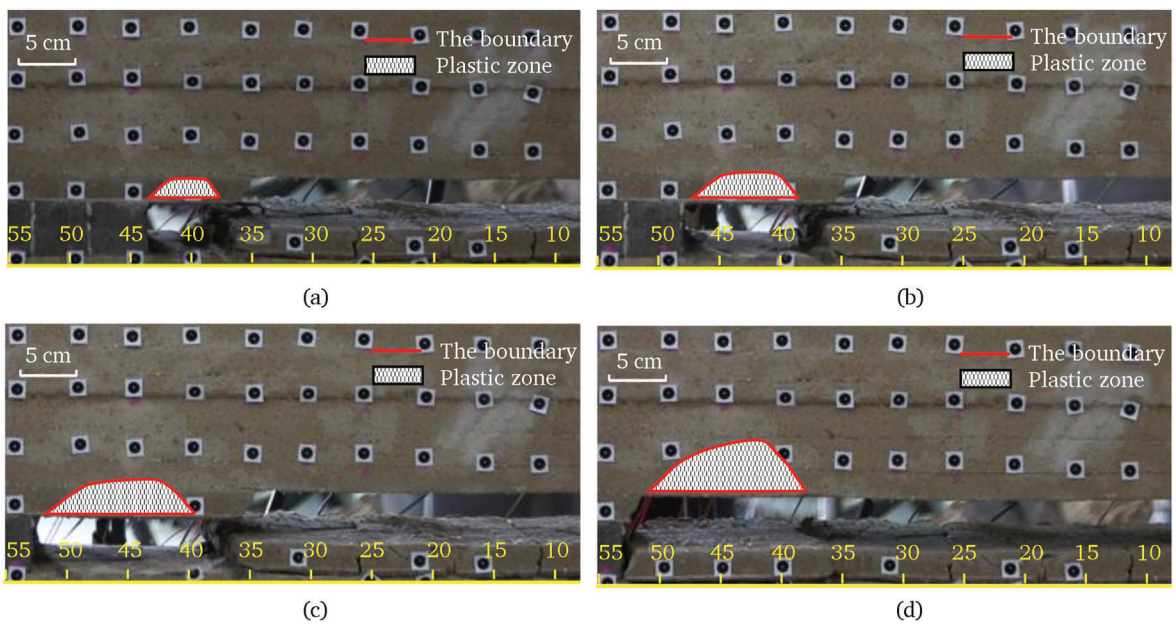

Fig. 21. Comparison between mechanical model and physical model during period caving of overburden roof (unit: cm). (a) Advancement distance 45 cm; (b) Advancement distance 50 cm; (c) Advancement distance 55 cm; (d) Advancement distance 55 cm.

similarity materials and laboratory condition. The mixing ratios of the model materials used in this physical experiment are presented in Table 2.

The model is laid at a height of 2 cm each time. Basing on different mixing ratios of rock strata, the amounts of similar materials used for a height of 2 cm is shown in Table 3. The laying height of the physical model is strictly carried out according to the geometric size of different rock strata, and an appropriate amount of mica powder is added to simulate the joint between rock layers.

Combined with the in-situ stress results of 21221 mining face in Qianqiu coal mine, the maximum and minimum principal stress are the horizontal stress, and the intermediate principal stress is the vertical stress and its lateral pressure coefficient is 1.17. Therefore, boundary stresses of 0.14 MPa, 0.14 MPa and 0.12 MPa are applied to the left, right and top boundary of the physical model respectively. When similar materials are laid in the physical model, twenty-two strain gauges are embedded in the rock strata to monitor the stress evolution of overburden roof during the coal seam mining, as shown in Fig. 17.

5.2. The phenomenon of overburden roof caving

To mitigate boundary effects, protective coal pillars were retained on both lateral sides of the physical model, with a total mining advance distance of 110 cm. The overburden deformation and caving behavior during coal seam extraction are visualized in Fig. 18.

The roof caving phenomenon was observed multiple times during the advancement process of coal seam mining, as shown in Fig. 18. These roof caving occurred at specific intervals along the mining face, namely at distances of 40 cm, 55 cm, 70 cm, 90 cm and 110 cm. Each roof caving had varying heights, measuring 2 cm, 6 cm, 6 cm, 14 cm and 36 cm, respectively. With the advancement of the mining face, the overburden roof gradually showed bent and sinking, the separation layer gradually developed and extended from roof bottom to roof top. The overlying strata above the stope showed trapezoidal collapse phenomenon, and the collapse height of overlying strata rise slowly. The caving intervals and caving heights of the roof varied significantly, indicating continuous and unstable failure of the overburden.

5.3. Validation of the mechanical models

This section aims to validate the rationality of the mechanical model by conducting a comparative analysis. Specifically, the stress distribution of the overburden roof obtained from the physical simulation experiment is compared with the theoretical derivation result. And the

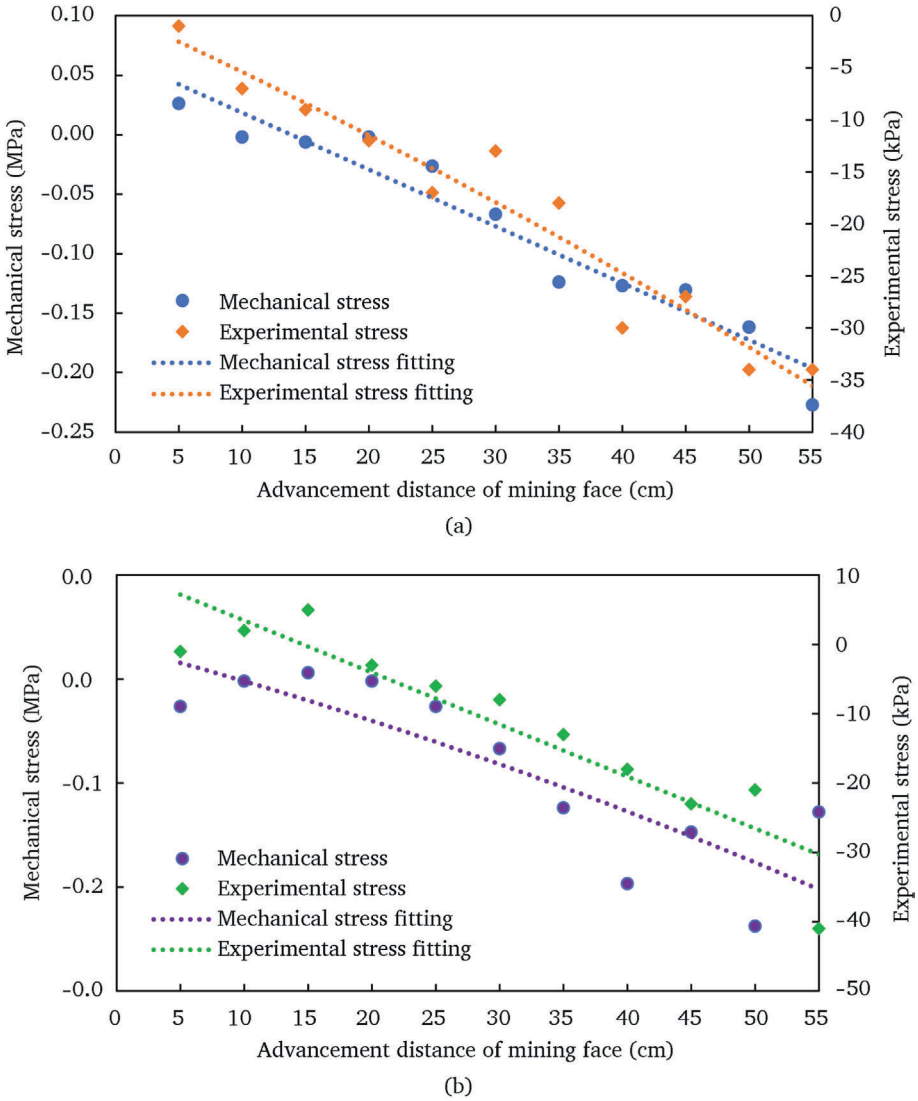

Fig. 22. Stress comparison between mechanical model and physical experiment during period caving of overburden roof. (*a*) 6# stress monitoring point; (*b*) 7# stress monitoring point.

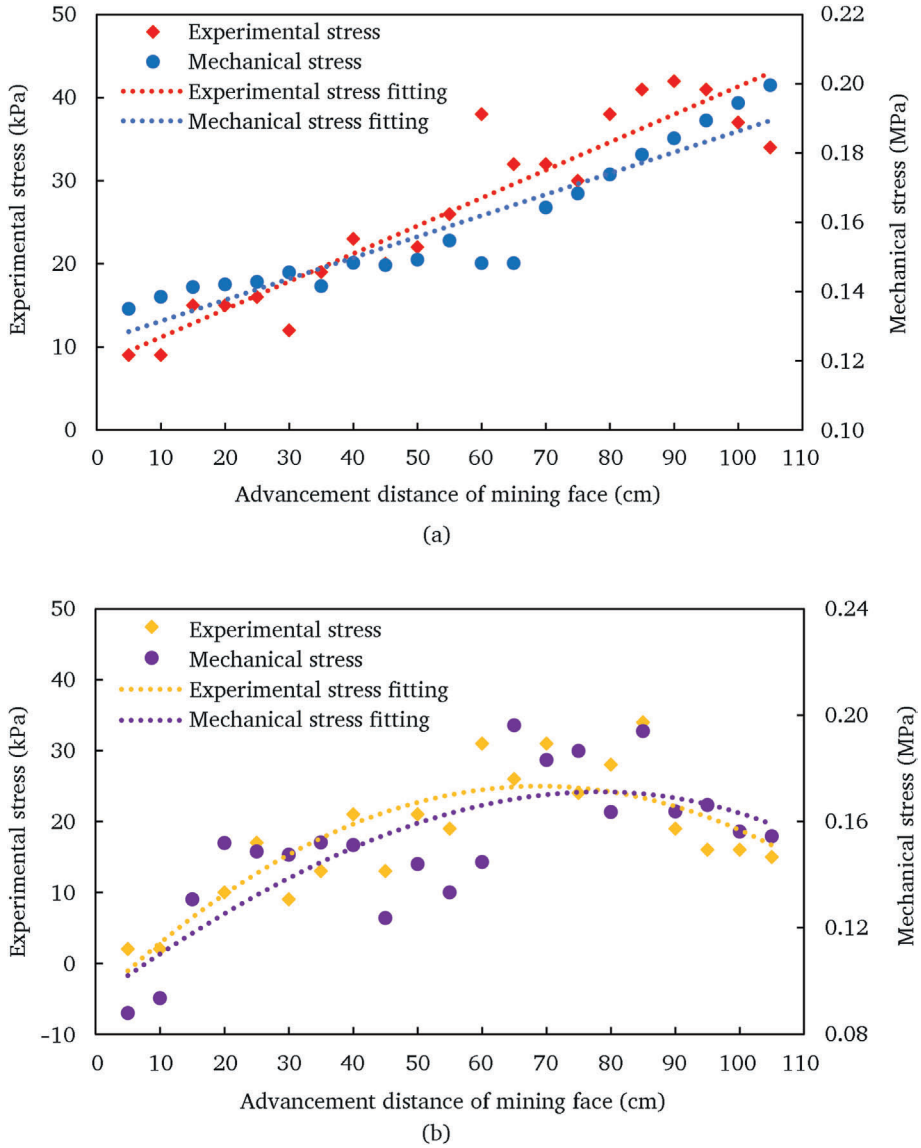

Fig. 23. Stress comparison of overburden roof between complex functions model and physical experiment. (a) 12# stress monitoring point; (b) 15# stress monitoring point.

results of the physical experiment and numerical simulation are also compared with the mechanical models in terms of the collapse area of overburden roof and the critical length for the overburden roof caving. This comparative analysis serves to assess the consistency and accuracy of the mechanical model in representing the behavior of the overburden roof during coal seam mining.

5.3.1. Comparison for the first caving of overburden roof

The overburden rock caving phenomenon in physical experiment is compared with the evolution of elastic-plastic boundary line and plastic zone in mechanical model, as shown in Fig. 19.

Drawing from the theoretical analysis of mechanical models during different stages of caving, the plastic zone emerges as a key indicator for characterizing the caving area of the roof. Specifically, the region beneath the elastic-plastic boundary line represents the plastic zone, signifying the portion of overburden rock that has already yielded and is susceptible to potential caving. However, it is important to note that the presence of a plastic zone does not necessarily mean that the overburden will collapse immediately. Whether the plastic zone will collapse needs to be determined by combining with the caving mechanical discriminating conditions of overburden roof. The area above the elastic-plastic boundary is the elastic zone, which has stable elastic deformation of overburden roof. The boundary line gradually extends from the middle of the overburden roof to both sides of the overburden roof during the coal seam mining. This indicates that overburden roof plastic zone first appears in the middle and low of the roof, which is consistent with the deformation characteristics of overburden roof, as shown in Fig. 19. It can be found that the boundary line form is symmetric about the middle of the model.

When mining face advances to 5 cm, neither plastic zone nor elastic-plastic boundary line is observed. With the continued advancement of mining face, overburden roof partial area near the goaf gradually enters the plastic deformation state from the elastic deformation state, and the elastic-plastic boundary begins to appear and gradually expands. It can be found that the plastic zone expands significantly along the vertical direction when the mining face advances to 30 cm. When the mining face continues advancing 10 cm, the scope of elastic-plastic boundary line and the plastic zone are also further expanded along the advancing direction of the mining face. The first caving of overburden rock occurs in the physical model, and combined with the calculation method of the critical length for the first caving of overburden roof, the critical length for the first caving is 42.5 cm. Therefore, regarding to the first caving of

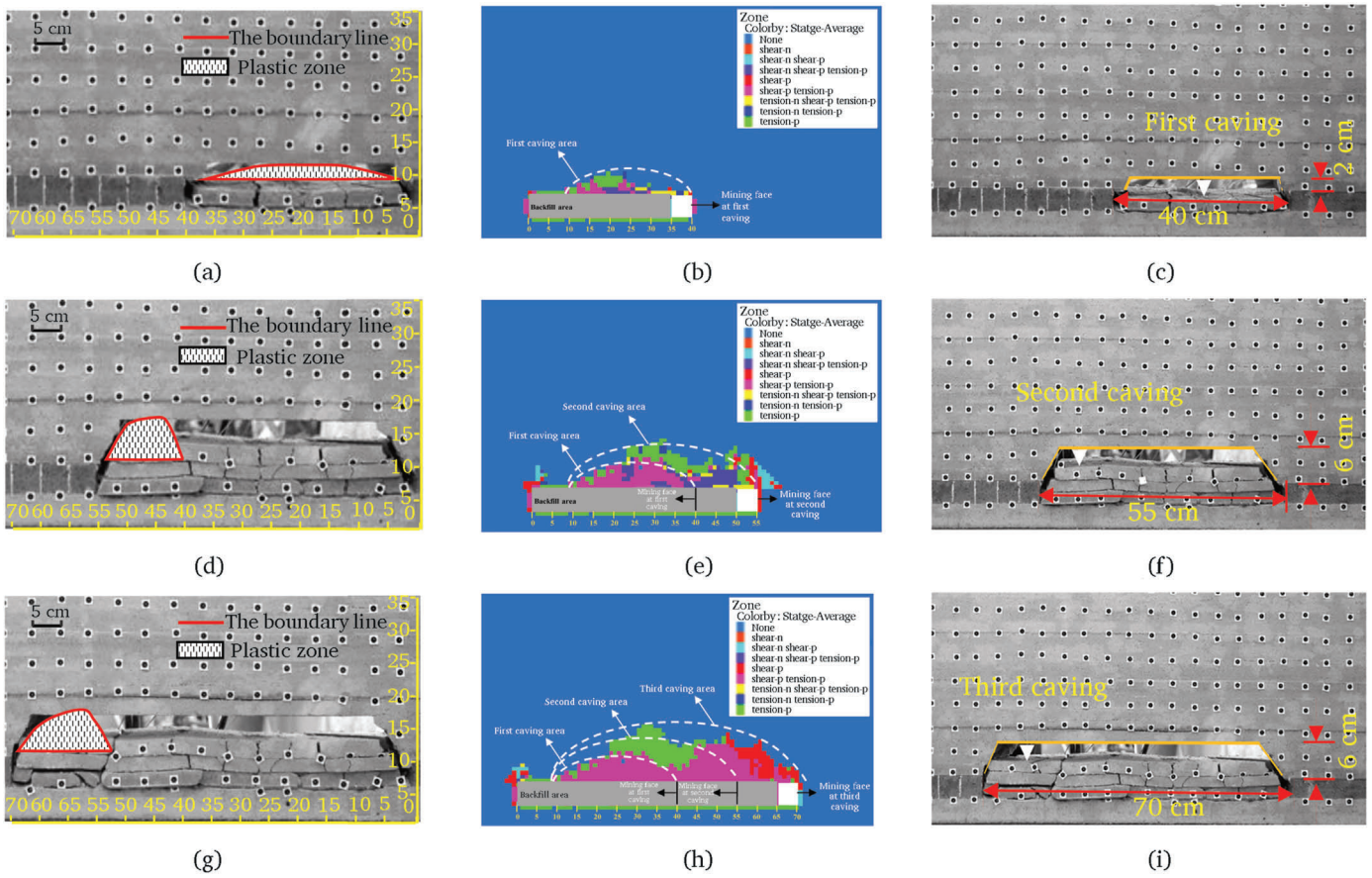

Fig. 24. Process comparison of overburden roof caving. (a) Mining distance 40 cm in theoretical model; (b) mining distance 40 m in numerical model; (c) mining distance 40 cm in physical model; (d) mining distance 55 cm in theoretical model; (e) mining distance 55 m in numerical model; (f) mining distance 55 cm in physical model; (g) mining distance 70 cm in theoretical model; (h) mining distance 70 m in numerical model; (i) mining distance 70 cm in physical model.

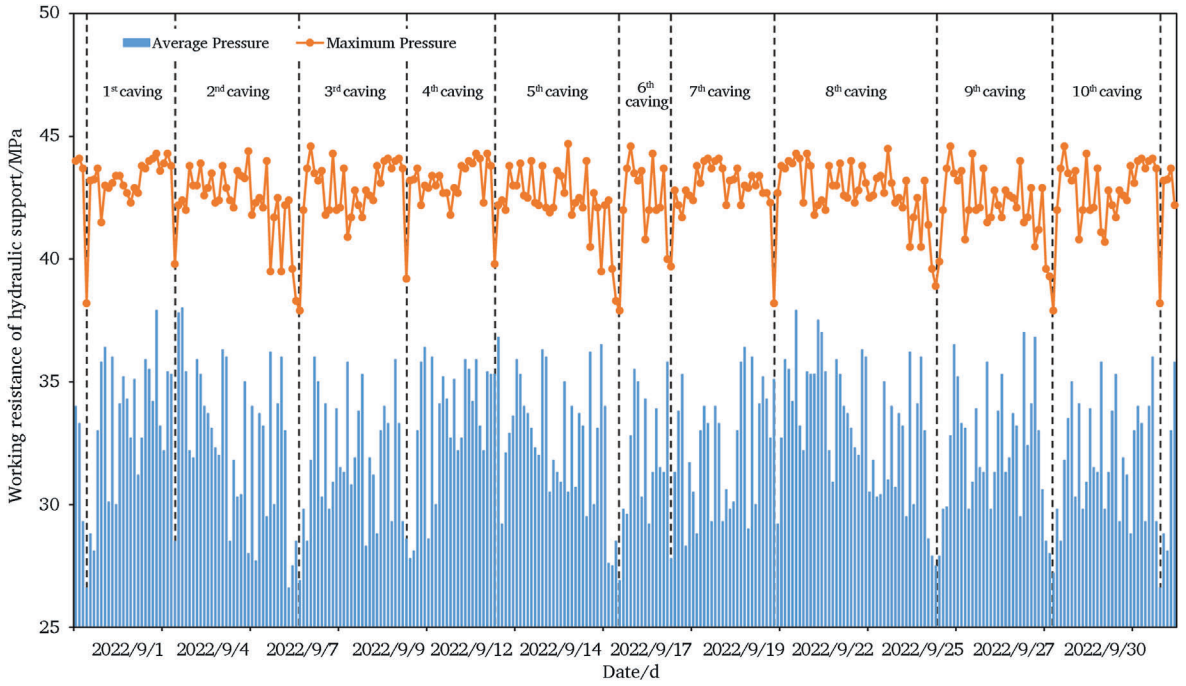

Fig. 25. Working resistance curve of 130–150# in mining face 21221 in September 2022.

overburden roof, the critical length theoretical result is in good agreement with the advancing distance of the mining face in the physical model.

In the physical model, the first caving of overburden roof occurs when the mining face advances 40 cm, and the roof length is applicable to the mechanical model of first caving of the overburden roof is also 40 cm. Combined with the location of 22 stress monitoring points in the physical model, it can be seen that only 1#–5# stress monitoring points can be used to compare the stress change with that in the mechanical model of first caving. It should be noted that 4# stress monitoring point is accidently damaged during the experiment process.

During 40 cm advancement distance of mining face, the theoretical stress calculated by the mechanical model of first caving is compared with the stress monitored from the physical model, as shown in Fig. 20. It can be seen that the variation trends of theoretical stress and experimental stress of 1#–3#, 5# monitoring points are in good agreement, indicating that the stress distribution calculated by the mechanical model of first caving is basically consistent with that monitored from the physical model.

5.3.2. Comparison for the periodic caving of overburden roof

Following the first caving of the overburden roof, it transitions into several periodic caving stages, each characterized by a distinct mechanical model that differs from the first caving. Therefore, it is crucial to conduct a comparative analysis between the periodic caving phenomenon observed in the physical experiment and the corresponding mechanical model, as shown in Fig. 21.

The boundary line gradually extends from the middle of the overburden roof to left, and right side of the overburden roof during the coal seam mining, as shown in Fig. 21. It can be found that the boundary line form is asymmetric at the middle of the model. This indicates that the deformation of the overburden roof during periodic caving is no longer symmetrical, which is different from that of the overburden roof during first caving. The elastic-plastic boundary line and plastic zone in the mechanics model of first caving of the overburden roof begin to appear near the rock strata above the goaf when the mining face advances 5 cm. When the mining face continues to advance 15 cm, the plastic zone shows significant expansion along the advancement direction. Combined with the calculation formula of the critical length for the periodic caving of overburden roof, the critical length for the periodic caving in the mechanical model is 16.4 cm.

In the physical experiment, the periodic caving of overburden roof occurs when the mining face continues to advance 15 cm. Therefore, the roof length applicable to the mechanical model of periodic caving is also 15 cm. Combined with 22 stress monitoring points in the physical experiment, 6# and 7# stress monitoring points are selected to compare the stress change with that in the mechanical model of periodic caving as shown in Fig. 22. It can be seen that the stress variation trends of theoretical model and experimental model at 6# and 7# monitoring points show identical performance, indicating that the stress distribution calculated by the mechanical model of periodic caving is basically consistent with the stress distribution monitored in the physical model test.

5.3.3. Comparison for the complex functions model of overburden roof

When the first caving and multiple periodic caving of the lower rock strata occur successively, the upper rock strata will also collapse and form a large caving area. The stress distribution in the large caving area is complicated at this time. Therefore, during the mining face advances 105 cm, the theoretical stress calculated by the complex functions model was chosen to compare with the stress measured by 12# and 15# stress monitoring points in the physical model test, as shown in Fig. 23. The variation trends of theoretical stress and experimental stress at 12# and 15# monitoring points are in good agreement. With the continuous advancement of the mining face, the stress of 12# monitoring point continues to increase, but the stress of 15# monitoring point presents first slow increase and then gradual decrease.

Quantitative comparison of mining advance distances demonstrates excellent congruence among numerical simulations, theoretical predictions, and physical model test results, as shown in Fig. 24, validating the consistency of multi-methodological approaches in characterizing mining-induced roof behavior. In terms of the caving morphology of overburden roof, it is evident that the caving span of rock strata in both numerical simulation and physical model tests are relatively similar. However, there is a noticeable difference in caving height between the two methods. This is because in the physical experiments the rock layers, which are made of similar simulation materials, are placed in layers of 2 cm each. This deliberate layering makes the collapse of the rock strata easier. However, such layering settings are not presented in the numerical simulation.

Fig. 25 illustrates the working resistance curve of the hydraulic support monitored by the ground pressure station at the 21221 mining face from September 1 to September 30, 2022. As shown in the picture, a total of 10 periodic roof weighting events were observed in September, with an average periodic weighting interval of 15.7 m. This field measurement demonstrates close agreement with the critical length of 16.4 m for the periodic roof caving deduced by the complex functions mechanical model.

6. Conclusions

In this study, the stress distribution in the overburden rock strata is obtained by the complex functions model. The main conclusions are listed as follows:

(1) Through the establishment of the complex functions model, the stress distribution of the rock strata outside the caving area is obtained. In the complex functions model of overburden roof, the stress components σ_x, σ_y, τ_{xy} and σ_θ distribution of overburden roof all firstly increase and then gradually decrease, and finally stay stable with the increase of the horizontal distance from the center of the fracture zone. The peak values of these stress components present the characteristics of an obvious increase with the increase of ratios of model length to height. With the increase of lateral pressure coefficient, the peak value of stress component σ_x presents obviously increase, σ_y, τ_{xy} and σ_θ present obviously decrease.
(2) According to the different boundary conditions at the two ends of the rock beam, different superstatic beam mechanics models are established to solve the stress evolution inside the overburden caving area. Through theoretical derivation, stress evolution patterns of overburden strata at different caving stages were derived under both elastic and elastoplastic deformation conditions, accompanied by the demarcation of elastic-plastic zones. In addition, the mechanical discriminant condition for overburden rock caving is proposed, the critical length for the first caving and periodic caving of overburden are determined.
(3) Utilizing the stress distribution results derived from the mechanical models, a mechanical identification criteria has been established to accurately identify and assess the caving behavior of overburden roof. A numerical algorithm, utilizing continuous medium response and employing the FLAC^{3D} is developed, enabling dynamic simulation for the first caving and periodic caving of the overburden roof during the advancement of the mining face. Furthermore, the numerical results and field measurement demonstrates are found to be in agreement with the results observed in the theoretical, validating the accuracy and reliability of the complex functions model.
(4) Physical model tests were conducted to investigate the deformation and failure characteristics of overburden roof during the mining face advances. By studying the dynamic evolution of stress in the mining area, the relationship between stress

evolution and caving process of overburden roof is determined. To validate the proposed analytical framework, quantitative comparisons between theoretical analyses, numerical results and experimental were performed in terms of the caving range of roof strata, the critical length for the roof strata caving and stress distribution. The consistencies among different approaches confirms the reliability of the theoretical model.

CRediT authorship contribution statement

Yinkai Li: Writing – original draft, Data curation, Writing – review & editing, Formal analysis. **Hongwei Wang:** Methodology, Formal analysis, Writing – review & editing, Funding acquisition. **Zhanbin Zhu:** Validation, Data curation, Investigation. **Daixin Deng:** Software, Formal analysis, Methodology, Data curation. **Naisheng Jiang:** Methodology, Writing – review & editing.

Declaration of competing interest

The authors declare the following financial interests/personal relationships which may be considered as potential competing interests: Zhanbin Zhu is currently employed by Mataihao Coal Mine, Inner Mongolia Ordos Yongmei Mining Industry Co., Ltd., China.

Acknowledgements

This study was financially supported by the State Key Research Development Program of China (2024YFC3013804); the Independent Research fund of Joint National-Local Engineering Research Center for Safe and Precise Coal Mining (Anhui University of Science and Technology) (EC2022001); National Natural Science Foundation of China (41872205); Beijing Natural Science Foundation (8202041); State Key Laboratory for Geomechanics and Deep Underground Engineering, China University of Mining & Technology, Beijing (XDJJ2020001-006).

Abbreviations

F_{16}	Thrust fault in Yima mining area
UCS	Uniaxial compressive strength
$FLAC^{3D}$	Fast Lagrangian Analysis of Continua in 3 dimensions

References

Alehossein, H., Poulsen, B.A., 2010. Stress analysis of longwall top coal caving. Int. J. Rock Mech. Min. Sci. 47, 30–41. https://doi.org/10.1016/j.ijrmms.2009.07.004.

Alejano, L.R., Taboada, J., García-Bastante, F., Rodriguez, P., 2008. Multi-approach back-analysis of a roof bed collapse in a mining room excavated in stratified rock. Int. J. Rock Mech. Min. Sci. 45 (6), 899–913. https://doi.org/10.1016/j.ijrmms.2007.10.001.

Deng, D.X., Wang, H.W., Xie, L.L., Wang, Z.L., Song, J.Q., 2023. Experimental study on the interrelation of multiple mechanical parameters in overburden rock caving process during coal mining in longwall panel. Int. J. Coal Sci. Technol. 10, 47. https://doi.org/10.1007/s40789-023-00608-2.

Deng, D.X., 2023. Study on Stress Field Evolution Characteristics of Overburden Rock Deformation and Failure in Mining Face of Coal Mine. Dissertation. China University of Mining and Technology, Beijing (in Chinese).

Deng, G.D., Xie, H.P., Gao, M.Z., Xie, J., Li, C., He, Z.Q., 2023. Fracture mechanisms of competent overburden under high stress conditions: a case study. Rock Mech. Rock Eng. 56, 1759–1777. https://doi.org/10.1007/s00603-022-03169-z.

He, M.C., Gong, W.L., Li, D.J., Zhai, H.M., 2009. Physical modeling of failure process of the excavation in horizontal strata based on IR thermography. Min. Sci. Technol. 19, 689–698 (in Chinese).

He, M.C., Ren, S.L., Guo, L.J., Lin, W.J., Zhang, T.W., Tao, Z.G., 2022. Experimental study on influence of host rock strength on shear performance of Micro-NPR steel bolted rock joints. Int. J. Rock Mech. Min. Sci. 159, 105236. https://doi.org/10.1016/j.ijrmms.2022.105236.

Huang, Q.X., 2002. Ground pressure behavior and definition of shallow seams. Chin. J. Rock Mech. Eng. 21 (8), 1174–1177 (in Chinese).

Huang, Q.X., 2007. Experimental research of overburden movement and subsurface water seeping in shallow seam mining. J. Univ. Sci. Technol. Beijing 14 (6), 483–489. https://doi.org/10.1016/S1005-8850(07)60114-5.

Jiang, H., Dou, L.M., Gong, S.Y., Li, J., Ma, Z.Q., 2017. Rock burst assessment and prediction by dynamic and static stress analysis based on micro-seismic monitoring. Int. J. Rock Mech. Min. Sci. 93, 46–53. https://doi.org/10.1016/j.ijrmms.2017.01.005.

Jiang, Y.D., Pan, Y.S., Jiang, F.X., Dou, L.M., Ju, Y., 2014. State of the art review on mechanism and prevention of coal bumps in China. J. China coal. Soc. 39 (2), 205–213 (in Chinese).

Jiang, Y.D., Zhao, Y.X., 2015. State of the art: investigation on mechanism, forecast and control of coal bumps in China. Chin. J. Rock Mech. Eng. 34 (11), 2188–2204 (in Chinese).

Kumar, R., Singh, A.K., Mishra, A.K., Singh, R., 2015. Underground mining of thick coal seams. Int. J. Min. Sci. Technol. 25 (6), 885–896. https://doi.org/10.1016/j.ijmst.2015.09.003.

Le, T.D., Oh, J., Hebblewhite, B., Zhang, C.G., Mitra, R., 2018. A discontinuum modelling approach for investigation of longwall top coal caving mechanisms. Int. J. Rock Mech. Min. Sci. 106, 84–95. https://doi.org/10.1016/j.ijrmms.2018.04.025.

Li, X.M., Wang, Z.H., Zhang, J.W., 2017. Stability of roof structure and its control in steeply inclined coal seams. Int. J. Min. Sci. Technol. 27 (2), 359–364. https://doi.org/10.1016/j.ijmst.2017.01.018.

Liu, C., Liu, Z.H., Zhang, J.W., Yang, Z.Q., Cai, Z.C., Li, Y.L., 2018. Effect of mining face length on the evolution of spatial structure of overlying strata and the law of underground pressure in large mining height face. Rock soil. Mech 39 (2), 691–698 (in Chinese).

Liu, J.K., Li, C.Y., Shi, Y.Y., Zhang, Y., 2021. Stability analysis and fracture patterns of hard main roof in longwall top coal caving with large mining height. Hindawi 2021, 9930221. https://doi.org/10.1155/2021/9930221.

Lou, J.F., Gao, F.Q., Yang, J.H., Ren, Y.F., Li, J.Z., Wang, X.Q., Yang, L., 2021. Characteristics of evolution of mining-induced stress field in the longwall panel: insights from physical modeling. Int. J. Coal Sci. Technol. 8, 938–955. https://doi.org/10.1007/s40789-020-00390-5.

Lv, H.Y., Cheng, Z.B., Liu, F., 2021. Study on the mechanism of a new fully mechanical mining method for extremely thick coal seam. Int. J. Min. Sci. Technol. 142, 104788. https://doi.org/10.1016/j.ijrmms.2021.104788.

Miao, K.J., Tu, S.H., Liu, X., Ji, X.Z., 2021. Large deformation analysis and control of retaining entry along the backfilling working face with thick hard roof in deep mining. J. China Coal Soc. 46 (4), 1232–1241 (in Chinese).

Qian, M.G., 1981. A study of the behaviour of overlying strata in longwall mining and its application to strata control. Dev. Geotech. Eng. 32, 13–17.

Qian, M.G., Miu, X.X., He, F.L., 1994. Analysis of key block in the structure of voussoir beam in longwall mining. J. China Coal Soc. 19 (6), 557–563 (in Chinese).

Qian, M.G., Miu, X.X., Xu, J.L., 1996. Theoretical study of key stratum in ground control. J. China Coal Soc. 21 (3), 225–230 (in Chinese).

Shabanimashcool, M., Li, C.C., 2015. Analytical approaches for studying the stability of laminated roof strata. Int. J. Rock Mech. Min. Sci. 85 (79), 99–108. https://doi.org/10.1016/j.ijrmms.2015.06.007.

Shen, B.T., Yi, D., Xun, L., van de Werken, M., Dlamini, B., Chen, L., Vardar, O., Canbulat, I., 2020. Monitoring and modelling stress state near major geological structures in an underground coal mine for coal burst assessment. Int. J. Rock Mech. Min. Sci. 129, 104294. https://doi.org/10.1016/j.ijrmms.2020.104294.

Song, Z.Q., 1994. Basic research of key techniques related to decision-making in mine safety. J. China Coal Soc. 19 (1), 1–4 (in Chinese).

Wang, H.J., Liu, D., Cui, Z.D., Cheng, C., Jian, Z., 2016. Investigation of the fracture modes of red sandstone using XFEM and acoustic emissions. Theor. Appl. Fract. Mech. 85, 283–293. https://doi.org/10.1016/j.tafmec.2016.03.012.

Wang, H.W., Xue, S., Shi, R.M., Jiang, Y.D., Gong, W.L., Mao, L.T., 2020. Investigation of fault displacement evolution during extraction in longwall panel in an underground coal mine. Rock Mech. Rock Eng. 53, 1809–1826. https://doi.org/10.1007/s00603-019-02015-z.

Wang, H.W., Wang, Z.L., Jiang, Y.D., Song, J.Q., Jia, M.N., 2022. New approach for the digital reconstruction of complex mine faults and its application in mining. Int. J. Coal Sci. Technol. 9, 43. https://doi.org/10.1007/s40789-022-00506-z.

Wang, J.C., Xu, J.L., Yang, S.L., Wang, Z.H., 2023. Development of strata movement and its control in underground mining: in memory of 40 years of Voussoir beam theory proposed by academician minggao qian. Coal Sci. Technol. 51 (1), 80–89 (in Chinese).

Wen, Z.J., Tang, J.Q., Wang, H.B., 2011. Study on mechanical model and hydraulic support working state in mining stope with large mining height. J. China Coal Soc. 36 (S1), 42–46 (in Chinese).

Xia, B.W., Jia, J.L., Yu, B., Zhang, X., Li, X.L., 2017. Coupling effects of coal pillars of thick coal seams in large-space stopes and hard stratum on mine pressure. Int. J. Min. Sci. Technol. 27 (6), 965–972. https://doi.org/10.1016/j.ijmst.2017.06.020.

Xu, J.L., Qian, M.G., Zhu, W.B., 2005. Study on influences of primary key stratum on surface dynamic subsidence. Chin. J. Rock Mech. Eng. 24 (5), 787–791 (in Chinese).

Xu, Z.L., 2016. Elastic Mechanics, fifth ed. Higher Education Press, Beijing.

Yang, S.L., Zhang, J.W., Chen, Y., Song, Z.Y., 2016. Effect of upward angle on the drawing mechanism in longwall top-coal caving mining. Int. J. Rock Mech. Min. Sci. 85, 92–101. https://doi.org/10.1016/j.ijrmms.2016.03.004.

Yuan, L., Jiang, Y.D., He, X.Q., Dou, L.M., Zhao, Y.X., Zhao, X.S., Wang, K., Yu, Q., Lu, X.M., Li, H.C., 2018. Research progress of precise risk accurate identification and monitoring early warning on typical dynamic disasters in coal mine. J. China Coal Soc. 43 (2), 306–318 (in Chinese).

Zhang, S.K., Lu, L., Wang, Z.M., Wang, S.D., 2021. A physical model study of surrounding rock failure near a fault under the influence of footwall coal mining. Int. J. Coal Sci. Technol. 8, 626–640. https://doi.org/10.1007/s40789-020-00380-7.